# Effects of composition and phase relations on mechanical properties and crystallization of silicate glasses

KILINC, Erhan <http://orcid.org/0000-0002-5280-0275>, BELL, Anthony M. T., BINGHAM, Paul A. and HAND, Russell J.

Received: 23 December 2020 | Revised: 17 February 2021 | Accepted: 17 February 2021

DOI: 10.1111/jace.17784

Journal of the American Ceramic Society

ORIGINAL ARTICLE

# Effects of composition and phase relations on mechanical properties and crystallization of silicate glasses

**Erhan Kilinc**[1,2,3] | **Anthony M. T. Bell**[1] | **Paul A. Bingham**[1] | **Russell J. Hand**[2]

[1]Materials and Engineering Research Institute, College of Business, Science and Technology, Sheffield Hallam University, Sheffield, UK

[2]Department of Materials Science and Engineering, University of Sheffield, Sheffield, UK

[3]LAV&Gurallar Container Glass, Kutahya, Turkey

**Correspondence**
Erhan Kilinc, Materials and Engineering Research Institute, College of Business, Science and Technology, Sheffield Hallam University, Sheffield S1 1WB, UK.
Email: e.kilinc@shu.ac.uk

**Abstract**

Crystallization, mechanical properties, and workability are all important for the commercialization and optimization of silicate glass compositions. However, the interrelations of these properties as a function of glass composition have received little investigation. Soda-lime-silica glasses with $Na_2O$-MgO-CaO-$Al_2O_3$-$SiO_2$ compositions relevant to commercial glass manufacture were experimentally studied and multiple liquidus temperature and viscosity models were used to complement the experimental results. Liquidus temperatures of the fabricated glasses were measured by the temperature gradient technique, and Rietveld refinements were applied to X-Ray powder diffraction (XRD) data for devitrified glasses, enabling quantitative determination of the crystalline and amorphous fractions and the nature of the crystals. Structural properties were investigated by Raman spectroscopy. Acoustic echography, micro-Vicker's indentation, and single-edge-notched bend testing methods were used to measure Young's moduli, hardness, and fracture toughness, respectively. It is shown that it is possible to design lower-melting soda-lime-silica glass compositions without compromising their mechanical and crystallization properties. Unlike Young's modulus, brittleness is highly responsive to the composition in soda-lime-silica glasses, and notably low brittleness values can be obtained in glasses with compositions in the wollastonite primary phase field: an effect that is more pronounced in the silica primary phase field. The measured bulk crystal fractions of the glasses subjected to devitrification at the lowest possible industrial conditioning temperatures indicate that soda-lime-silica glass melts can be conditioned close to their liquidus temperatures within the compositional ranges of the primary phase fields of cristobalite, wollastonite, or their combinations.

**KEYWORDS**

crystallization, mechanical properties, soda-lime-silica glass

## 1 | INTRODUCTION

Many technological properties of glasses are intrinsically related to their chemical compositions and many studies have previously reported significant variations in mechanical and physical properties of glasses due to compositional modifications. For example, studies are available which link the indentation cracking behavior of glasses to Poisson's ratio,

Young's modulus, and hardness.[1] Furthermore, plastic deformation as a material response to applied stress is reported to be very small in silicate glasses.[2] Nonetheless, the presence of smaller ionic radii cations can enhance plastic deformation at the crack tip and consequently increase the fracture toughness of oxide glasses.[3] On the other hand, silicate glasses have been reported with low brittleness values, attributed to their enhanced network densification capacity and higher molar volumes.[4] In addition, patents have been granted claiming tougher and more scratch-resistant silicate glasses, obtained by minimization of the proportion of non-bridging oxygen atoms in the network.[5] However, other studies have shown a lack of clear association between network connectivity and fracture toughness.[6,7] Overall, no universal mechanisms based on glass composition have been identified linking one material property to another.

The number of studies aimed at exploring any significant connections between the crystallization behavior of glasses, such as the primary crystalline phase field and the mechanical properties, is small. Babcock[8] correlated the coefficient of thermal expansion and refractive index with the primary crystalline phase field of different types of silicate glasses. Subsequently, Georoff and Babcock[9] proposed that silicate glasses contain ordered or arrayed substructures which structurally mimic their primary crystalline phases and they established a relationship between hardness and the primary phase field of silicate glasses. Further to this, the nonlinear variation of brittleness in soda-lime-silica glass was reported by Deriano et al[7] to be linked with transitions from one crystalline phase field to another.

Suitable processing parameters are essential to produce a viable commercial glass from carefully designed compositions, and the liquidus temperature and the rate of crystallization are key processing parameters that require the utmost attention during design, testing, and validation of any new commercial glass compositions. One of the first studies investigating the compositional dependency of the crystallization properties of soda-lime-silica type glasses was conducted by Morey,[10] who established the fundamental primary phase field diagram for $Na_2O$-CaO-$SiO_2$ glass systems and thereafter modified the phase field boundaries by systematic boron oxide additions.[11] Subsequently the influence of $Al_2O_3$ additions on the crystallization characteristics of glasses in the $Na_2O$-CaO-$SiO_2$ and $Na_2O$-MgO-CaO-$SiO_2$ systems was investigated in depth by Silverman.[12,13] However, wollastonite or diopside, which are the primary phase fields of some silicate glasses, were lacking in those studies. In addition to liquidus temperature, the rate of crystal growth is also a very important technological parameter, particularly for float glass manufacture, and the work of Swift[14] clearly identified the role of the phase field in determining the rate of crystal growth in soda-lime-silica type glasses, but the corresponding glass series were either lacking MgO or included insignificant amounts of $Al_2O_3$. Similarly, low $Al_2O_3$ concentrations were present in the glasses studied by Owens-Illinois[15-17] for which the influence of various oxides on liquidus temperature and primary phase field were investigated. On the other hand, more recent work by Hrma et al[18] investigated the crystallization properties of MgO- and $Al_2O_3$-bearing commercial float glass-like quaternary compositions in a narrow compositional range. Nonetheless they observed broad variations in liquidus temperatures and in the primary crystalline phases. Similarly, MgO- and $Al_2O_3$-containing low melting container glass quaternary compositions were designed and studied by Bingham and Marshall[19] based on their liquidus and forming temperatures. However, the number of such studies is small, and the majority of soda-lime-silica glass compositions in the literature for which the crystallization properties have been investigated do not fully represent the modern complex soda-lime-silica systems ($Na_2O$-MgO-CaO-$Al_2O_3$-$SiO_2$) typical of current industrial practice.

In this study, a qualitative approach was taken to examine the inter-relations of mechanical properties, crystallization behavior, and workability of soda-lime-silica glasses as functions of composition and crystal phase field. The behavior of mechanical and crystallization properties of quinary soda-lime-silica glasses were investigated by replacing CaO or MgO for $SiO_2$; MgO for CaO; and $SiO_2$ with equimolar amounts of $Na_2O$ and $Al_2O_3$. X-Ray diffraction data for heat-treated glasses, as well as Raman spectra of glassy states, were collected to gain further insight into the measured variations in mechanical and crystallization properties of these glasses. Various liquidus temperature models from literature were also considered alongside experimental liquidus temperature and crystal phase field measurements, and the attempt was made to establish associations between primary crystal phase field and mechanical properties, whilst also enabling assessment of the accuracy of each liquidus model within this system. Finally, brittleness values were examined as a function of melting and liquidus temperatures of the studied complex soda-lime-silica glasses.

## 2 | EXPERIMENTAL PROCEDURE

### 2.1 | Sample preparation

Four series of glasses (labeled MS, CS, MC, and ASN) were produced. In the MS and CS glass series, MgO/$SiO_2$ and CaO/$SiO_2$ molar ratios were modified, respectively. In the MC glass series, the MgO/CaO ratio was modified. Glasses of the ASN series were produced by varying the [$Al_2O_3$ + $Na_2O$]/[$SiO_2$] molar ratio with $Na^+$ charge compensating $[AlO_4]^-$ units. In all four glass series, nominal molar concentrations of other components remained constant. The nominal compositions of glasses of the CS glass series were $13.5Na_2O{\cdot}(7+x)CaO{\cdot}3MgO{\cdot}1.5Al_2O_3{\cdot}(75-x)SiO_2$ (mol%) where $x = 0$, 1,

2, 3, 4, 5, 6, 7 (glasses coded as $C_{(7+x)}S_{(75-x)}$); those of the MS glass series $13.5Na_2O{\cdot}10CaO{\cdot}yMgO{\cdot}1.5Al_2O_3{\cdot}(75-y)SiO_2$ (mol%) where $y$ = 0, 1, 2, 3, 4, 5, 6, 7 (glasses coded as $M_yS_{(75-y)}$); those of the MC glass series $13.5Na_2O{\cdot}(13-z)CaO{\cdot}(z)MgO{\cdot}1.5Al2O3{\cdot}72SiO_2$ (mol %) where $z$ = 1, 3, 5, 7, 9, 11 (glasses coded as $M_zC_{(13-z)}$)., the molar concentration of $Na_2O$ was also modified in proportion to the change in $Al_2O_3$ concentration and those of the ASN glass series $(12+w)\ Na_2O{\cdot}10CaO{\cdot}3MgO{\cdot}wAl_2O_3{\cdot}(75-2w)SiO_2$ (mol %) where $w$ = 0, 0.5, 1.5, 2.5, 3.5, and 4.5 (glasses coded as $A_wS_{(75-2w)}N_{(12+w)}$).

Batches were weighed to produce 300 g of glass using $SiO_2$ sand (>99.5%), $Na_2CO_3$ (> 99.1%), $CaCO_3$ (> 99.3%) (Supplied by Glassworks Services), $Na_2SO_4$ (Acros Organics, >99.0%), $4MgCO_3{\cdot}Mg(OH)_2{\cdot}5H_2O$, and $Al(OH)_3$ (both supplied by Fischer Scientific; purities >99.0%). In most cases, approximately 1/30 of the target $Na_2O$ content was supplied by $Na_2SO_4$ which was present in the batch as a refining agent for the glass melt. The thoroughly mixed batch was transferred into a zirconia grain-stabilized platinum (ZGS-Pt) crucible and melted in an electric furnace at 1450°C for 5 hours. After allowing 1 hour to obtain a batch-free melt, a motorized Pt stirrer was lowered into the melt and switched on, stirring the glass melt for a further 4 hours to ensure a homogenous glass melt. Finally, the molten glass was poured into a pre-heated steel mold and allowed to cool until stiff. After demolding, the glass was transferred to an annealing furnace to anneal at the annealing temperatures predicted by a global statistical glass viscosity model of Fluegel[20] (on the basis of nominal glass compositions, see Table 7) for 1 hour, then cooled to room temperature at a rate of 1°C/min.

As-annealed bulk glass blocks were cut into samples of 20 × 20 × 3 mm dimensions, using a Buehler ISOMET 5000. The samples were ground using successive MetPrep SiC abrasive papers (120, 240, 400, 600, 800, and 1200 grits) and thereafter were polished using MetPrep diamond solutions (6 μm, 3 μm oil based, and 1 μm water based) to obtain a mirror-like surface finish. In order to relieve residual stresses due to machining, grinding, and polishing, glass specimens were then heated to their predicted annealing temperature at a rate of 1°C/min then cooled down to room temperature at a rate of 1°C/min after a 1 hour dwell at the annealing temperature. The re-annealed specimens were examined under a polariscope to ensure that the residual stresses had been removed by the re-annealing.

## 2.2 | Chemical and physical property measurements

The oxide compositions of the as-produced glasses were measured using the fusion method on a calibrated X-ray fluorescence (XRF) program by Glass Technology Services Ltd, Sheffield, UK (Table 1). Estimated experimental errors are ±0.5 wt% for major oxides such as $SiO_2$ which may range between 65–77 wt%; ±0.15 wt% for the oxides which may range between 12–17 wt%; and ±0.12 wt% for the oxides where the content of each was between 6.0–12 wt%; and less than ±0.1 wt% for the levels of each oxide less than 6.0 wt%. Densities were obtained by using an electronic density meter (Mettler TOLEDO™ New Classic *MS*) which uses Archimedes principle. Specimens were cleaned with isopropanol to remove any debris prior to measurement, and were placed in distilled water of known temperature. Five independent measurements were averaged to calculate the mean density of each glass.

The packing density ($C_g$) of atoms within a glass can be calculated using[21]

$$C_g = \rho \frac{\sum (Z_i J_i)}{\sum (J_i M_i)} \quad (1)$$

where $Z_i$ is equal to $\frac{4}{3}/\pi N_A \left(xr_A^3 + yr_B^3\right)$ for the $i^{th}$ oxide with a chemical formula of $A_xB_y$. $N_A$ is Avogadro's number, $J_i$ and $M_i$ are molar fraction and molar mass of the $i^{th}$ constituent in glass, respectively. $r_A$ and $r_B$ are the ionic radii, and Shannon's[22] tabulated ionic radius values were used to calculate the packing density of atoms within the studied glasses. $\rho$ is the density of glass.

Molar volume ($V_M$) of the glass series was calculated using[21]:

$$V_M = \frac{\sum (J_i M_i)}{\rho} \quad (2)$$

## 2.3 | Structural property measurement

### 2.3.1 | Liquidus temperature measurement

Liquidus temperature can be defined as the highest temperature at which melt and the primary crystalline phase can coexist at equilibrium.[23] In this study, the temperature at which the first crystal grain observed was considered to be the liquidus temperature of the glass. Liquidus temperatures were measured using the gradient boat method,[24] wherein ~10 grams of glass sample was crushed in a stainless steel mortar and transferred into either alumina (from Almath® BS91) or platinum (from Sigma Aldrich Z685429) boats. Glass samples were held in the furnace for 24 hours within a known temperature gradient and then quenched in air to cool to room temperature. Liquidus temperatures of the glass samples were determined by observing the devitrification within the bulk glass using an Alicona Infinite Focus optical microscope. For all studied glass compositions, the difference between two independent liquidus temperature measurements was less than 5°C, hence the cumulative error in measured liquidus temperature, including other systematic errors, was

**TABLE 1** Normalized XRF data of glass compositions in weight and molar %. Batched glass compositions for ASN glass series were $(12 + w)Na_2O{\cdot}10CaO{\cdot}3MgO{\cdot}wAl_2O_3{\cdot}(75\text{-}2w)SiO_2$ (mol %) where $w = 0$, 0.5, 1.5, 2.5, 3.5, and 4.5, and for MS glass series $13.5Na_2O{\cdot}10CaO{\cdot}yMgO{\cdot}1.5Al_2O_3{\cdot}(75–y)SiO_2$ (mol%) where $y = 0$, 1, 2, 3, 4, 5, 6, 7, and for CS glass $13.5Na_2O{\cdot}(7 + x)CaO{\cdot}3MgO{\cdot}1.5Al_2O_3{\cdot}(75–x)SiO_2$ (mol%) where $x = 0$, 1, 2, 3, 4, 5, 6, 7, and for MC glass series $13.5Na_2O{\cdot}(13–z)CaO{\cdot}zMgO{\cdot}1.5Al_2O_3{\cdot}72SiO_2$ (mol %) where $z = 1$, 3, 5, 7, 9

| Glass Series | Glass ID | | $SiO_2$ | $Al_2O_3$ | $Na_2O$ | MgO | CaO | $Fe_2O_3$ |
|---|---|---|---|---|---|---|---|---|
| ASN | $A_0S_{75}N_{12}$ | Mol% | 75.32 | 0 | 11.39 | 2.93 | 10.33 | 0.03 |
| | | Wt% | 76.27 | 0 | 11.9 | 1.99 | 9.76 | 0.08 |
| | $A_{0.5}S_{74}N_{12.5}$ | Mol% | 74.39 | 0.43 | 11.92 | 2.89 | 10.34 | 0.03 |
| | | Wt% | 75.07 | 0.74 | 12.41 | 1.96 | 9.74 | 0.08 |
| | *$A_{1.5}S_{72}N_{13.5}$* | *Mol%* | *72.19* | *1.52* | *12.88* | *2.98* | *10.4* | *0.03* |
| | | *Wt%* | *72.31* | *2.58* | *13.31* | *2* | *9.72* | *0.08* |
| | $A_{2.5}S_{70}N_{14.5}$ | Mol% | 70.49 | 2.11 | 14.2 | 2.87 | 10.3 | 0.03 |
| | | Wt% | 70.25 | 3.57 | 14.6 | 1.92 | 9.58 | 0.08 |
| | $A_{3.5}S_{68}N_{15.5}$ | Mol% | 69 | 2.84 | 15.16 | 2.78 | 10.19 | 0.03 |
| | | Wt% | 68.41 | 4.78 | 15.5 | 1.85 | 9.43 | 0.04 |
| | $A_{4.5}S_{66}N_{16.5}$ | Mol% | 66.76 | 3.55 | 16.41 | 2.93 | 10.32 | 0.03 |
| | | Wt% | 65.85 | 5.94 | 16.7 | 1.94 | 9.5 | 0.08 |
| MS | $M_0S_{75}$ | Mol% | 74.87 | 1.49 | 13.28 | 0 | 10.33 | 0.03 |
| | | Wt% | 74.26 | 2.51 | 13.59 | 0 | 9.56 | 0.08 |
| | $M_1S_{74}$ | Mol% | 74.06 | 1.52 | 13.51 | 1 | 9.89 | 0.03 |
| | | Wt% | 73.65 | 2.56 | 13.86 | 0.67 | 9.18 | 0.08 |
| | $M_2S_{73}$ | Mol% | 73 | 1.48 | 13.31 | 1.88 | 10.29 | 0.04 |
| | | Wt% | 72.85 | 2.51 | 13.7 | 1.26 | 9.58 | 0.11 |
| | *$M_3S_{72}$* | *Mol%* | *72.19* | *1.52* | *12.88* | *2.98* | *10.4* | *0.03* |
| | | *Wt%* | *72.31* | *2.58* | *13.31* | *2* | *9.72* | *0.08* |
| | $M_4S_{71}$ | Mol% | 70.77 | 1.52 | 13.45 | 3.83 | 10.4 | 0.03 |
| | | Wt% | 71.07 | 2.59 | 13.93 | 2.58 | 9.75 | 0.08 |
| | $M_5S_{70}$ | Mol% | 69.64 | 1.51 | 13.76 | 4.82 | 10.23 | 0.04 |
| | | Wt% | 70.15 | 2.58 | 14.29 | 3.26 | 9.62 | 0.11 |
| | $M_6S_{69}$ | Mol% | 68.95 | 1.54 | 13.34 | 5.8 | 10.33 | 0.03 |
| | | Wt% | 69.69 | 2.64 | 13.91 | 3.93 | 9.75 | 0.08 |
| | $M_7S_{68}$ | Mol% | 68.06 | 1.45 | 13.29 | 6.76 | 10.39 | 0.04 |
| | | Wt% | 69.04 | 2.5 | 13.91 | 4.6 | 9.84 | 0.11 |
| CS | $C_7S_{75}$ | Mol% | 75.58 | 1.45 | 12.81 | 2.89 | 7.24 | 0.03 |
| | | Wt% | 75.56 | 2.46 | 13.21 | 1.94 | 6.76 | 0.08 |
| | $C_8S_{74}$ | Mol% | 73.83 | 1.49 | 13.58 | 2.83 | 8.25 | 0.01 |
| | | Wt% | 73.83 | 2.53 | 14.01 | 1.9 | 7.7 | 0.03 |
| | $C_9S_{73}$ | Mol% | 73.14 | 1.54 | 13.1 | 2.88 | 9.31 | 0.03 |
| | | Wt% | 73.16 | 2.62 | 13.51 | 1.93 | 8.7 | 0.08 |
| | *$C_{10}S_{72}$* | *Mol%* | *72.19* | *1.52* | *12.88* | *2.98* | *10.4* | *0.03* |
| | | *Wt%* | *72.31* | *2.58* | *13.31* | *2* | *9.72* | *0.08* |
| | $C_{11}S_{71}$ | Mol% | 71.01 | 1.51 | 13.06 | 2.96 | 11.43 | 0.03 |
| | | Wt% | 71.17 | 2.57 | 13.5 | 1.99 | 10.69 | 0.08 |
| | $C_{12}S_{70}$ | Mol% | 70.18 | 1.49 | 13.15 | 2.87 | 12.27 | 0.03 |
| | | Wt% | 70.36 | 2.54 | 13.6 | 1.93 | 11.49 | 0.08 |
| | $C_{13}S_{69}$ | Mol% | 69 | 1.52 | 13.24 | 2.87 | 13.34 | 0.03 |
| | | Wt% | 69.21 | 2.59 | 13.7 | 1.93 | 12.49 | 0.08 |

(Continues)

**TABLE 1** (Continued)

| Glass Series | Glass ID | | $SiO_2$ | $Al_2O_3$ | $Na_2O$ | MgO | CaO | $Fe_2O_3$ |
|---|---|---|---|---|---|---|---|---|
| | $C_{14}S_{68}$ | Mol% | 68.04 | 1.48 | 13.23 | 2.87 | 14.34 | 0.05 |
| | | Wt% | 68.29 | 2.52 | 13.7 | 1.93 | 13.43 | 0.13 |
| MC | $M_1C_{12}$ | Mol% | 72.08 | 1.26 | 13.5 | 1 | 12.13 | 0.03 |
| | | Wt% | 71.93 | 2.13 | 13.9 | 0.67 | 11.3 | 0.08 |
| | *$M_3C_{10}$* | *Mol%* | *72.19* | *1.52* | *12.88* | *2.98* | *10.4* | *0.03* |
| | | *Wt%* | *72.31* | *2.58* | *13.31* | *2* | *9.72* | *0.08* |
| | $M_5C_8$ | Mol% | 72.75 | 1.18 | 13.07 | 4.76 | 8.2 | 0.04 |
| | | Wt% | 73.35 | 2.02 | 13.59 | 3.22 | 7.72 | 0.11 |
| | $M_7C_6$ | Mol% | 73.04 | 1.17 | 12.91 | 6.66 | 6.19 | 0.03 |
| | | Wt% | 74.03 | 2.01 | 13.5 | 4.53 | 5.86 | 0.08 |
| | $M_9C_4$ | Mol% | 72.6 | 1.22 | 13.13 | 8.89 | 4.12 | 0.04 |
| | | Wt% | 73.98 | 2.11 | 13.8 | 6.08 | 3.92 | 0.11 |
| | $M_{11}C_2$ | Mol% | 72.13 | 1.26 | 13.53 | 11.01 | 2.03 | 0.03 |
| | | Wt% | 73.91 | 2.19 | 14.3 | 7.57 | 1.94 | 0.08 |

Glasses of each series are presented in the form of $A_wS_{(75-2w)}N_{(12+w)}$, $M_yS_{(75-y)}$, $C_{(7+x)}S_{(75-x)}$, and $M_zC_{(13-z)}$ for ASN, MS, CS, and MC glass series, respectively. For reader convenience base glass composition is denoted by different glass codes as $A_{1.5}S_{72}N_{13.5}$, $M_3S_{72}$, $C_{10}S_{72}$, and $M_3C_{10}$ in four glass series (italicized in table).

conservatively estimated to be ±10°C, and this also appears to be in line with the measurement error estimated by the standard.[24] However, crystallization of one glass sample, $M_{11}C_2$ in the MC series, was not observed under optical microscopy for dwell times of either 24 and 48 hours; therefore the length of time to obtain equilibrium for this glass was extended to 168 hours to enable the detection of crystals under optical microscopy.

### 2.3.2 | X-ray powder diffraction

At least 5·0 g samples of all glasses were placed into an Au-stabilized Pt crucible and heated to a temperature ~30°C below its measured liquidus temperature, at a heating rate of 10°C/min, and held at this temperature for 48 hours to grow crystalline phases and identify them in situ by X-Ray powder Diffraction (XRD). Finally, samples were quenched in air to cool to the room temperature. Devitrified glass samples were then removed from the crucible, and samples of devitrified glass were ground for 15 seconds with a rotation rate of 700 rpm in an automated stainless steel mortar. Powdered devitrified glass samples were loaded into flat-plate sample holders prior to room temperature XRD data collection. XRD data were collected using the PANalytical X'Pert MPD (Cu$K\alpha$ X-rays used) and the PANalytical Empyrean (Co$K\alpha$ X-rays used) diffractometers. These XRD data showed large amorphous "humps" with some sharper Bragg reflections, suggesting that the samples had a large amorphous content. To determine the percentages of amorphous material and crystalline phase/s present in each sample a known amount of NIST 640e silicon standard material was added as an internal standard. XRD data were then re-collected with these silicon-containing samples, and data analyzed using the PANalytical HighScore Plus software and the International Centre for Diffraction Data Powder Diffraction File[25] to determine the crystalline phases present (including silicon). Rietveld refinements[26] were then carried out (using FULLPROF[27]) from these data to determine the proportions of phases in the crystalline component in each sample. From the difference in the known weight percentage of silicon added to the sample and the weight percentage of silicon in the crystalline component, it was possible to determine the percentage amorphous content of each sample.[28]

### 2.3.3 | Structural analysis

Structural analysis of the produced glasses was carried out using Raman spectroscopy. Raman spectra of all glasses were acquired using a Renishaw InVia Raman Spectrometer. The spectrometer was calibrated using a Si wafer reference standard prior to measurement. Excitation of the polished and annealed glass surfaces was performed with a laser of wavelength of 514.5 nm at a laser power of 20 mW.A × 50 objective lens was used to deliver the laser beam and focused at a depth just beneath the polished surface. The exposure and acquisition times were both set to 10 seconds. The raw data were transferred to Labspec software and a baseline fitted by linearly connecting four points where the spectra reaches zero following

the method of Colomban et al,[29] and thereafter the baseline was subtracted from the spectra. For spectral normalization, the method of Le Losq et al[30] was followed, and the intensity of each spectrum was divided by the total area under that spectrum.

## 2.4 | Mechanical property measurements and calculations

### 2.4.1 | Hardness

Micro-Vicker's indentation was used to determine the hardness of the glasses. Vicker's indentations were produced on the polished surface of glass specimens from an applied force of 9.81 N for 20 seconds using a Mitutoyo Vickers indenter. The number of indentations performed on each sample was ~10. Vicker's hardness of glasses was determined using[3]:

$$H_V = 1.8555\left(\frac{P}{d^2}\right) \tag{3}$$

where $P$ is the indentation load and measured in kilograms-force, and $d$ is the average diagonal length of the Vicker's impression.

### 2.4.2 | Elastic Moduli and Poisson's ratio

Ultrasonic longitudinal ($V_L$) and transverse ($V_T$) wave velocities were measured using an Olympus Epoch 6000 to obtain elastic moduli of the glasses. The round trip time of flight ($\tau$) of high-frequency waves through the sample thickness of ($L$) can be used to define the wave velocity ($V = 2L/\tau$). The frequencies of the delay line longitudinal and transverse transducers were 20 and 5 MHz, respectively. Glycerol and couplant gel were used in order to facilitate the transmission of sound waves between specimen and transducers.

The shear modulus, $G$, was obtained using:

$$G = \rho V_T^2 \tag{4}$$

where $\rho$ is the density.

Young's modulus, $E$, was obtained using:

$$E = \rho V_T^2 \frac{\left(3V_L^2 - 4V_T^2\right)}{\left(V_L^2 - V_T^2\right)} \tag{5}$$

In order to minimize the cumulative error, Poisson's ratio ($\upsilon$) and bulk modulus ($K$) were calculated directly from the wave velocities using, respectively:

$$v = \frac{\left(V_L^2 - 2V_T^2\right)}{2\left(V_L^2 - V_T^2\right)} \tag{6}$$

and

$$K = \rho\frac{\left(3V_L^2 - 4V_T^2\right)}{3} \tag{7}$$

### 2.4.3 | Bending fracture toughness

The surface crack in flexure (SCF) method was chosen to determine the flexural fracture toughness of each glass, following the procedure described in the BS-EN ISO-18756: 2005 standard.[31] In line with the standard, Knoop indentation was used to induce controlled flaws on the specimen surface to be placed in tension. The ideal indentation load was established by trial and error, and fractographic analysis showed that a 2 kg (19.62 N) indentation load was ideal for producing acceptable semi-elliptical cracks. As-annealed bulk glass blocks were cut into bars ~3.5 × 4.0 × 46 mm to produce bend test specimens, and the surface to be placed in tension was successively ground to a 600 grit finish. The bend specimens were annealed prior to performing indentation at the center of the 46 × 4.0 mm face to prevent potential notch tip blunting. Lateral cracks and further residual stresses can be generated by the indentation process, and these might alter stress intensity at the crack tip and thus lead to erroneous fracture toughness values.[32-35] Hence the standard recommends removing the residual stress zone by grinding the indented face of the bend specimen. On the other hand, extra residual stresses can be generated as a result of the grinding process.[32] In order to assess the influence of residual stresses on fracture toughness values, bend-test specimens were prepared as "as-indented" and "ground," and in accordance with the standard procedure, residual stresses due to indentation processes were eliminated by gently removing 20–25 μm of glass with a 600 grit SiC abrasive paper in a direction perpendicular to the Knoop indent long diagonal. Fracture toughness values obtained with the two conditions did not vary significantly. A Hounsfield TX0038 universal testing machine equipped with a four-point bend fixture with articulating rollers was used with inner and outer spans set to 20 mm and 40 mm, respectively. A drop of silicone oil was placed in the pre-crack to inhibit moisture-assisted slow crack growth. The approach speed of the loading nose was set to 0.25 mm/min, and the specimens were loaded to fracture at a rate of 0.5 mm/min. A total of 235 specimens were prepared across all glass compositions studied, and 181 specimens fractured properly from the controlled defect and therefore were analyzed further. The fracture toughness was calculated using:

$$K_{Ic} = Y_{max}\left[3PF/AL^2\right]\sqrt{a} \tag{8}$$

where $P$ denotes the break load in N, and $Y_{max}$ is the maximum stress intensity factor, $F$ is the four-point fixture moment arm in mm, $A$ is the width of plate in mm, $L$ is the depth of plate in mm, and $a$ is the depth of flaw in m (see Appendix-B for details of the evaluation of $Y_{max}$). Once the specimens were fractured, the geometry of the semi-elliptical cracks on the face of the fracture surfaces was characterized using a Buehler multi-focus tool on a Nikon Eclipse LV150 microscope equipped with Buehler OMNIMET 9.5 software. If the geometry of the studied pre-crack did not meet the requirements of Annex B in BS-EN ISO-18756: 2005, the result was rejected.

### 2.4.4 | Brittleness

Brittleness of each glass was calculated from the measured Vicker's hardness and fracture toughness values using[36]:

$$B = \frac{H_V}{K_{Ic}} \tag{9}$$

## 3 | MODELING VISCOSITY, WORKING PROPERTIES, AND LIQUIDUS TEMPERATURE OF GLASSES

High-temperature viscosity governs the refining of molten glass, along with proper glass redox number and refining agents. It also partly dictates the energy requirements for glass manufacture, hence efforts to reformulate or modify existing commercial glass compositions to provide lower viscosities and thereby achieve lower melting energies and lower $CO_2$ emissions.[19,37,38] Log ($\eta$/dPa-s) = 2 generally corresponds to a viscosity at melting temperature for most soda-lime-silica type glass compositions, and it is also regarded as the refining viscosity of molten glass. Liquidus viscosity[39] at log ($\eta$/dPa-s) = ~4 or alternatively liquidus temperature (denoted as $T_{Liq}$) can, to a degree, be interchangeably used to establish the crystallization properties of glass while new glass compositions are studied. The well-known concept of Working Range ($WR$) was established to control and predict the risk of devitrification of commercial container, tableware, float, and fiber glass compositions. For instance, the difference between forming temperature (denoted as $T_4$ and corresponding to $10^4$ dPa-s for container glass and denoted as $T_3$ corresponding to $10^3$ dPa-s for fiber forming processes) and liquidus temperature has been used as a practical approach to predict the risk of devitrification, and the greater the value of [$T_4 - T_{Liq}$] for container glass and [$T_3 - T_{Liq}$] for fiber glass the lower the likelihood of devitrification. On the other hand, viscosity values for inflow of the molten glass into the tin bath for float glasses, and for gob forming of container glasses, range between log ($\eta$/dPa-s) = 3.6–3.8 and 3.5–3.7, respectively.[37,40]

Various models have been developed to predict the high-temperature viscosity of glass. The Adam–Gibbs (AG), Avramov–Milchev, MYEGA (Mauro–Yue–Ellison–Gupta–Allan), and Vogel–Fulcher–Tammann (VFT) equations have all been used to model and predict low- and high-temperature viscosities of glass. Mauro et al[41] compared three of these models and demonstrated that the Avramov–Milchev and MYEGA models correctly yield convergence at the low-temperature limits, and the VFT and MYEGA models converge strongly in the high-temperature limit. On the other hand, the degree of divergence of the VFT equation is still low, and this model provides a good fit to the experimental dataset for viscosity values smaller than log ($\eta$/dPa-s) = ~11.[41] The VFT model is also by far the most widely used in the literature for commercial-type soda-lime-silica glasses. Fluegel[20] developed a model using a global statistical approach based on more than 2200 silicate composition–viscosity data from the scientific literature, and this model also correlates VFT constants to silicate glass composition. Hence Fleugel's viscosity model, combined with calculated VFT constants, was used to model the compositional dependence of viscosity between log ($\eta$/dPa-s) = 2 and 5, relating to the viscosities associated with melting, refining, conditioning, and forming of commercial silicate glasses.

Some of the models developed by Cuartas,[42] Babcock,[43] Šašek et al,[44] Karlsson et al,[45] and Fluegel[46] have been commonly used to estimate the liquidus temperature of silicate glasses. The liquidus model developed by Babcock[43] is a function of $SiO_2$, $Al_2O_3$, CaO, and $Na_2O$ concentrations, whereas MgO is lacking in this model. Furthermore, the other models, such as those developed by Cuartas[42] and Šašek et al.[44] are only valid for a small range of glass compositions. Additionally, a machine learning approach can also be used to predict the liquidus temperature of silicate glasses,[47] and such an approach may allow the prediction of more accurate liquidus temperature values, particularly for glass compositions crossing phase boundaries.

Karlsson et al[45] introduced the phase discriminator model ($P$-phase) which identifies the primary phase field of a glass, and accordingly the liquidus temperature can be calculated using the discrete models developed for the corresponding primary phase field. However, discrete models for the liquidus temperature in tridymite and cristobalite phase fields are lacking; and therefore, the $P$-phase model is not valid for glasses with compositions falling within these primary phase fields. The $P$-phase model was modified here, with respect to the range of glass compositions studied in this work, to give equation (10). The primary phase field

is wollastonite if $P$-phase ≤1.5; devitrite if 1.5 ≤ $P$-phase ≤2.5; and $Na_2O$-2CaO-3$SiO_2$ if 2.5 ≤ $P$-phase ≤3.5.

$$\begin{aligned} P-\text{phase} = {} & 20.2156+0.2104\times[\text{MgO}]+0.4932 \\ & \times[\text{Na}_2\text{O}]+0.1193\times[\text{CaO}]-1.1285 \\ & \times[\text{SiO}_2]-0.0069\times[\text{Na}_2\text{O}] \\ & \times[\text{Na}_2\text{O}]+0.0106\times[\text{SiO}_2]\times[\text{SiO}_2] \end{aligned} \quad (10)$$

where the terms in square brackets indicate the mass fraction of the relevant oxide.

The liquidus temperatures of the glasses were calculated as follows.

For glasses in the wollastonite phase field:

$$\begin{aligned} T_{\text{Liq}} = {} & 703.9090+13.3897\times[\text{MgO}]+34.7753 \\ & \times[\text{Al}_2\text{O}_3]-112.4500\times[\text{Na}_2\text{O}]+12.3114 \\ & \times[\text{SiO}_2]+4.1663\times[\text{Na}_2\text{O}] \\ & \times[\text{Na}_2\text{O}]+1.1945\times[\text{CaO}]\times[\text{CaO}] \end{aligned} \quad (11)$$

For glasses in the devitrite phase field:

$$\begin{aligned} T_{\text{Liq}} = {} & -1176.37+42.6270\times[\text{MgO}]+36.0791 \\ & \times[\text{Al}_2\text{O}_3]+45.2996\times[\text{CaO}]+20.0059 \\ & \times[\text{SiO}_2]+0.446271\times[\text{Na}_2\text{O}]\times[\text{Na}_2\text{O}] \end{aligned} \quad (12)$$

and for glasses in the $Na_2O$·2CaO·3$SiO_2$ phase field:

$$\begin{aligned} T_{\text{Liq}} = {} & 1847.46+10.4334\times[\text{MgO}]+19.8177 \\ & \times[\text{Al}_2\text{O}_3]-151.59\times[\text{Na}_2\text{O}]+75.7960 \\ & \times[\text{CaO}]+4.26746\times[\text{Na}_2\text{O}] \\ & \times[\text{Na}_2\text{O}]-3.07671\times[\text{CaO}]\times[\text{CaO}] \end{aligned} \quad (13)$$

## 4 | RESULTS AND DISCUSSION

### 4.1 | Influence of composition on liquidus temperature and crystal phase fields

Figure 1A–D show that the model developed by Fluegel[46] overall gives the best estimate of the experimentally determined liquidus temperatures for the glasses studied here, but the model does not yield a good fit for high-MgO glasses in the MC series that lie within the diopside primary phase field. Karlsson's model[45] tends to underestimate the liquidus

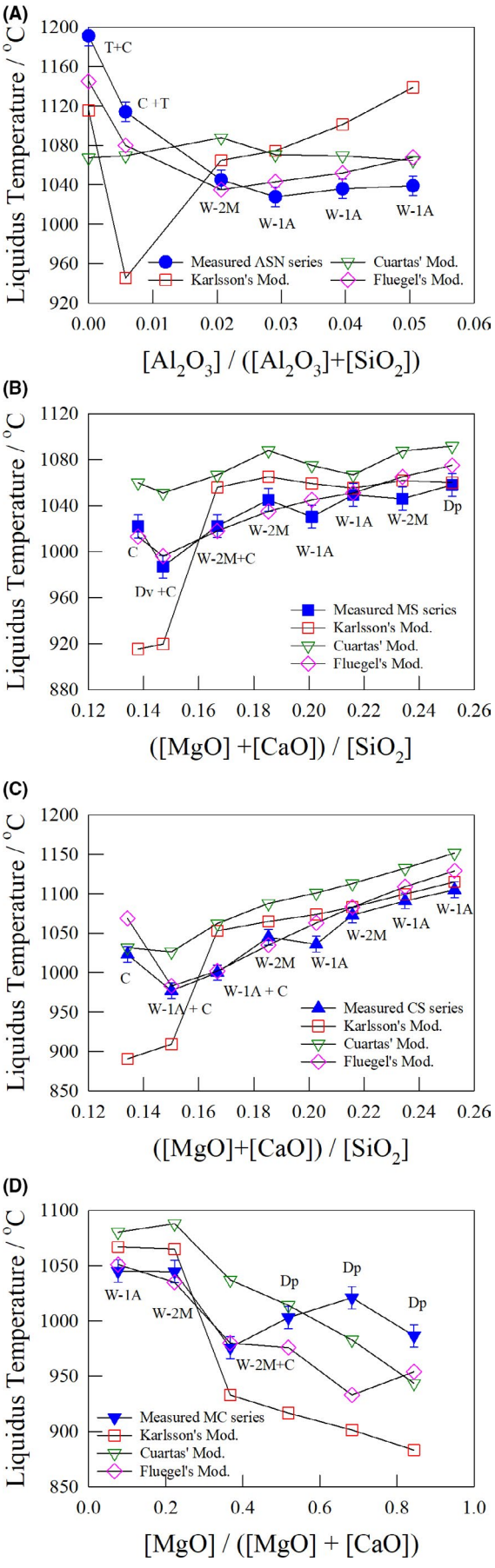


**FIGURE 1** Variation of liquidus temperatures and primary crystalline phases in (A) ASN glass series, (B) MS glass series, (C) CS glass series, and (D) MC glass series. *C*, *T*, *W*, *Dv*, and *Dp* stand for cristobalite, tridymite, different polytypes of wollastonite (*W-1A*, *W-2M*), devitrite, and diopside, respectively [Color figure can be viewed at wileyonlinelibrary.com]

**TABLE 2** Modeled and experimental crystal phase fields and liquidus temperatures of the studied glasses. *C*, *T*, *W*, *Dv*, and *Dp* stand for cristobalite, tridymite, wollastonite, devitrite, and diopside, respectively. *W-1A*, *W-2M* are the different polytypes of wollastonite

| Glass ID | Modeled primary phase field after Karlsson et al. (2002) | Determined Phase Fields | Measured Liquidus Temp. /°C | Modeled Liquidus Temperatures | | |
|---|---|---|---|---|---|---|
| | | | | Karlsson et al. (2002) /°C | Cuartas (1984) /°C | Fluegel (2007) /°C |
| $A_0S_{75}N_{12}$ | $N_1C_2S_3$ | T+C | 1191.0 | 1115.5 | 1067.5 | 1145.0 |
| $A_{0.5}S_{74}N_{12.5}$ | Dv | C+T | 1114.0 | 945.5 | 1069.5 | 1080.0 |
| **$A_{1.5}S_{72}N_{13.5}$** | **W** | **W-2M** | **1045.0** | **1065.0** | **1087.9** | **1035.0** |
| $A_{2.5}S_{70}N_{14.5}$ | W | W-1A | 1027.8 | 1074.6 | 1070.6 | 1043.0 |
| $A_{3.5}S_{68}N_{15.5}$ | W | W-1A | 1036.0 | 1101.2 | 1069.4 | 1052.0 |
| $A_{4.5}S_{66}N_{16.5}$ | W | W-1A | 1039.0 | 1138.8 | 1064.8 | 1068.0 |
| $M_0S_{75}$ | Dv | C | 1022.0 | 915.4 | 1059.8 | 1013.0 |
| $M_1S_{74}$ | Dv | Dv+C | 987.0 | 919.6 | 1051.0 | 996.0 |
| $M_2S_{73}$ | W | W-2M+C | 1022.3 | 1055.8 | 1066.5 | 1018.0 |
| **$M_3S_{72}$** | **W** | **W-2M** | **1045.0** | **1065.0** | **1087.9** | **1035.0** |
| $M_4S_{71}$ | W | W-1A | 1030.3 | 1059.2 | 1075.0 | 1045.0 |
| $M_5S_{70}$ | W | W-1A | 1049.3 | 1055.2 | 1066.7 | 1051.0 |
| $M_6S_{69}$ | W | W-2M | 1046.0 | 1061.8 | 1087.6 | 1065.0 |
| $M_7S_{68}$ | W | Dp | 1058.0 | 1060.0 | 1091.6 | 1075.0 |
| $C_7S_{75}$ | Dv | C | 1023.0 | 890.6 | 1031.7 | 1069.0 |
| $C_8S_{74}$ | Dv | C+W-1A | 977.0 | 909.4 | 1026.4 | 983.0 |
| $C_9S_{73}$ | W | W-1A+C | 1000.0 | 1053.0 | 1062.3 | 1002.0 |
| **$C_{10}S_{72}$** | **W** | **W-2M** | **1045.0** | **1065.0** | **1087.9** | **1035.0** |
| $C_{11}S_{71}$ | W | W-1A | 1036.0 | 1073.8 | 1101.1 | 1063.0 |
| $C_{12}S_{70}$ | W | W-2M | 1073.0 | 1083.1 | 1112.9 | 1083.0 |
| $C_{13}S_{69}$ | W | W-1A | 1091.0 | 1099.6 | 1132.4 | 1109.0 |
| $C_{14}S_{68}$ | W | W-1A | 1105.0 | 1115.0 | 1151.6 | 1129.0 |
| $M_1C_{12}$ | W | W-1A | 1045.0 | 1066.9 | 1080.3 | 1051.0 |
| **$M_3C_{10}$** | **W** | **W-2M** | **1045.0** | **1065.0** | **1087.9** | **1035.0** |
| $M_5C_8$ | Dv | W-2M+C | 976.0 | 933.0 | 1037.1 | 980.0 |
| $M_7C_6$ | Dv | Dp | 1003.0 | 916.8 | 1014.2 | 976.0 |
| $M_9C_4$ | Dv | Dp | 1021.0 | 901.4 | 982.8 | 933.0 |
| $M_{11}C_2$ | Dv | Dp | 986.6 | 883.3 | 943.7 | 954.0 |

For reader convenience the base glass composition is denoted by different glass codes namely $A_{1.5}S_{72}N_{13.5}$, $M_3S_{72}$, $C_{10}S_{72}$, and $M_3C_{10}$ in the four glass series (bold entries).

temperature values around the silica (*C*, *T*) and diopside primary phase fields, but gives relatively better fits in the wollastonite primary phase field. This can largely be attributed to the lack of variables for silica and diopside phase fields in Karlsson's phase discriminator model which therefore erroneously treats these phases as devitrite or $Na_2O{\cdot}2CaO{\cdot}3SiO_2$ (Table 2).

In general, and as might be expected, as the compositional range of the model validity broadens, deviations between the predicted and experimental liquidus temperatures also grow larger. The compositional range of the glasses studied in this work reasonably matches the range of validity of the nonlinear model of Cuartas[42] except for some of our high $SiO_2$(>73 wt%), CaO (>12.2 wt%), and MgO (>4.9 wt%) glasses; however, most of the modeled liquidus temperature values given by the Cuartas[42] model are significantly greater than the measured values. Nonetheless, despite this offset between modeled and measured values, the trends obtained using the model of Cuartas[42] are similar to the experimental trends within the wollastonite primary phase field of the glasses studied here.

In the ASN series of glasses, the measured molar ratios of $Na_2O$ /$Al_2O_3$ are greater than 1, and therefore the variation of liquidus temperature in this glass series is presented in terms of molar ratios of network-forming components aluminum oxide to silicon dioxide, albeit $SiO_2$ is replaced by equimolar

[$Na_2O + Al_2O_3$]. Figure 1A shows that the liquidus temperatures of the glasses in which $Al_2O_3$ is absent or very low are dramatically higher than those of the other $Al_2O_3$ bearing glasses. Their primary crystalline phase field is a mixture of tridymite and cristobalite, and additions of [$Na_2O + Al_2O_3$] reduce the liquidus temperatures of glasses within these silica phase fields, and thereafter, the liquidus temperature does not vary significantly and remains roughly constant with further substitution in the wollastonite phase field.

Figure 1B illustrates the variation of liquidus temperatures and primary crystalline phases as a result of molar replacement $SiO_2$ by MgO. The primary crystalline phase of MgO-free glass is cristobalite, and small additions of MgO initially move the primary phase field to devitrite, with larger MgO additions moving it to wollastonite. Diopside becomes the primary phase field for the MgO-rich end-member of the MS glass series. Initial additions of MgO into glass within the cristobalite primary phase field reduce the liquidus temperature, and further additions increase the liquidus temperature as the primary phase field shifts from devitrite to wollastonite. Liquidus temperature remains elevated for the glasses with diopside as the primary phase field.

The liquidus temperature decreases due to the initial addition of CaO to $C_7S_{75}$ glass, and then it begins to increase with further replacement, and therefore variation of liquidus temperature with replacement of $SiO_2$ by CaO in CS glass series shows similarities to the observed trends in the MS glass series (Figure 1C). Cristobalite is the primary crystalline phase in the lowest CaO containing $C_7S_{75}$ glass and wollastonite becomes the primary phase field due to the initial addition of CaO and remains unchanged as more CaO replaces $SiO_2$ for the rest of the CS glass series. Replacing $SiO_2$ by an equivalent amount of CaO or MgO gives rise to significant variation of liquidus temperatures across the range of compositions studied, and the highest liquidus temperatures are 1105 and 1058°C for CaO and MgO-rich end-member glasses, respectively.

Variation of liquidus temperature with exchange of alkaline earth oxides (MgO, CaO) does not exhibit a clear correlation in the MC glass series (Figure 1D). Initial additions of MgO do not change the primary phase field, and wollastonite remains the primary crystalline phase field. As more MgO replaces CaO, the primary phase field relocates in the neighborhood of wollastonite and cristobalite, and finally moves into the diopside primary phase field for the MgO-rich end-member. This indicates that the variation in liquidus temperature is sensitive to the primary phase transitions and reaches a minimum in the combination of wollastonite-*2M* and cristobalite phase fields and then increases again as the primary phase moves into the diopside primary phase field.

Although superimposition of quinary glass compositions on ternary phase diagrams has to be undertaken with caution, it does enable comparison of the position of the boundary lines of the glasses with those of reference systems, as was performed by Morey[11] for $B_2O_3$ containing silicate glasses, and Karlsson et al[45] who used this approach to compare the empirical and thermodynamic phase discriminator models with experimental data. The coordinates of the glass series in this work were plotted as a function of [$SiO_2$] and [CaO + MgO] contents on a weight basis in Morey's original $Na_2O$-CaO-$SiO_2$ phase diagram.[10] Figure 2 shows that the MS, CS, and MC glass series lie on the same master line, as opposed to the ASN glass series. Figure 2 also shows that the wollastonite primary phase field expands toward the devitrite and $Na_2O{\cdot}2CaO{\cdot}3SiO_2$ phase fields, and therefore the wollastonite phase field develops at much lower [CaO + MgO] concentrations in quinary silicate glass systems. Similarly, the formation of cristobalite takes place at much lower $SiO_2$ concentrations than those observed in Morey's $Na_2O$-CaO-$SiO_2$ system[10] and can coexist as a secondary phase field at much lower $SiO_2$ concentrations, for example, at 72.85 wt% in glass $M_2S_{73}$ in the MS glass series. In addition, Moir and Glasser[48] investigated the crystallization properties of soda-lime-silica glasses upon addition of $Al_2O_3$ to $SiO_2$-$Na_2O$-CaO ternary glasses, and comparing the 5 mol% $Al_2O_3$ isopleth of the $SiO_2$-$Na_2O$-CaO-$Al_2O_3$ system with the $Na_2O$-CaO-$SiO_2$ system of Shahid and Glasser[49] reveals that the addition of $Al_2O_3$ greatly expands the wollastonite phase field toward the tridymite and cristobalite fields, but

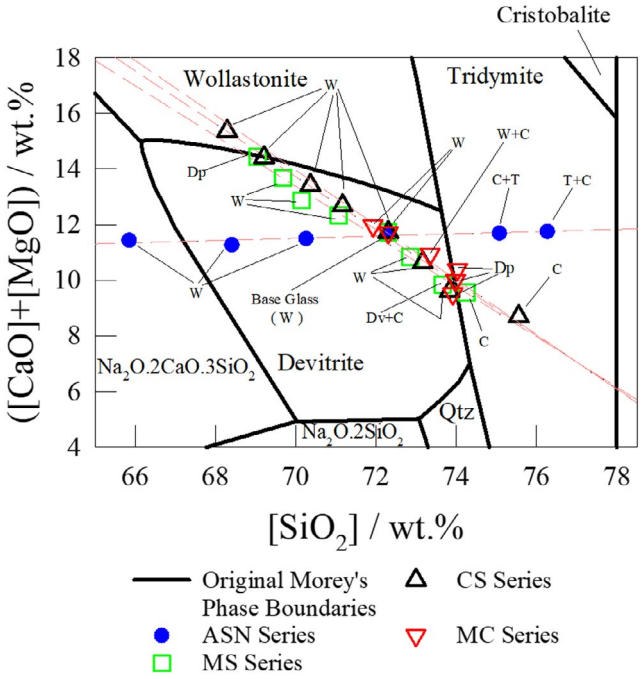


**FIGURE 2** The effect of substituting [$Al_2O_3$+$Na_2O$] for $SiO_2$; or CaO or MgO for $SiO_2$; or CaO with MgO on the boundaries of various phase fields on Morey's $Na_2O$-CaO-$SiO_2$ phase diagram.[10] *C*, *T*, *W*, *Dv*, *Dp*, and *Qtz* indicate cristobalite, tridymite, different polytypes of wollastonite (*W-1A*, *W-2M*), devitrite, diopside, and quartz, respectively [Color figure can be viewed at wileyonlinelibrary.com]

the boundaries of the devitrite phase field remain largely unchanged. On the other hand, the devitrite phase field no longer exists as a primary phase on the 10 mol% $Al_2O_3$ isopleth of the $Na_2O$-CaO-$Al_2O_3$-$SiO_2$ system and is replaced by plagioclase and $\beta$-wollastonite. Similarly, the work of Morey[50] also indicated that when substituting [$Na_2O$ + CaO + $SiO_2$] with $Al_2O_3$, the replacement of CaO by $Al_2O_3$ was dominant in transforming the primary phase field from tridymite to wollastonite. Overall, the addition of $Al_2O_3$ to $Na_2O$-MgO-CaO-$SiO_2$ glasses, as investigated here by the ASN glass series, expands the boundaries of the wollastonite phase field toward the silica phase fields, and this might be an explanation of the formation of wollastonite as a primary phase field with increasing $Al_2O_3$ concentrations in the samples from $A_{1.5}S_{72}N_{13.5}$ to $A_{4.5}S_{66}N_{16.5}$.

The work of Shahid and Glasser[51] indicates that the 5 mol % MgO isopleth of the $Na_2O$-MgO-CaO-$SiO_2$ system does not differ significantly from Morey's[10] $Na_2O$-CaO-$SiO_2$ system, although the wollastonite phase field slightly expands toward the $Na_2O{\cdot}2CaO{\cdot}3SiO_2$ phase field, and diopside develops as a primary phase field on the 10 mol% MgO isopleth of the system. It is probable that the diopside may have formed somewhere between the 5 and 10 mol% MgO isopleths of this system. Further to this, Morey[52] observed that the onset of transformation from $Na_2O{\cdot}3CaO{\cdot}6SiO_2$ to diopside occurs at ~7 mol% MgO in the $Na_2O$-MgO-CaO-$SiO_2$ system. The results of the current study also suggest that MgO behaves in a similar manner to CaO up to certain concentrations, as is observed in most of the MS and CS glass series, whose primary phase field remains wollastonite upon replacement of MgO or CaO for $SiO_2$. However, the diopside develops as a primary phase field with MgO concentrations from as low as 6.76 and 6.66 mol% in the MS and MC glass series, respectively. These reveal that the onset of diopside formation as a primary phase field may occur at MgO levels of 6-7 mol% in $Na_2O$-MgO-CaO-$SiO_2$ and $Na_2O$-MgO-CaO-$Al_2O_3$-$SiO_2$ systems, in agreement with Morey.[46]

## 4.2 | Variation of the rate of bulk crystallization with composition

It appears that the glassy phase fraction in the ASN glasses does not vary significantly with composition. The compositional dependence of the glassy phase fraction for the other devitrified glasses is deemed to be statistically significant as the uncertainties do not overlap completely. As is shown in Figure 5A-D, the glassy phase fraction of glasses obtained by Rietveld refinement of the XRD data varies between ~0.92 and ~0.99, (Figures 3 and 4) and these levels appear to be higher (~0.84 to ~0.90) than the measured values for devitrified float glass ($Na_2O$-CaO-MgO-$Al_2O_3$-$SiO_2$) compositions.[18] The float glass compositions studied by Hrma et al[18]

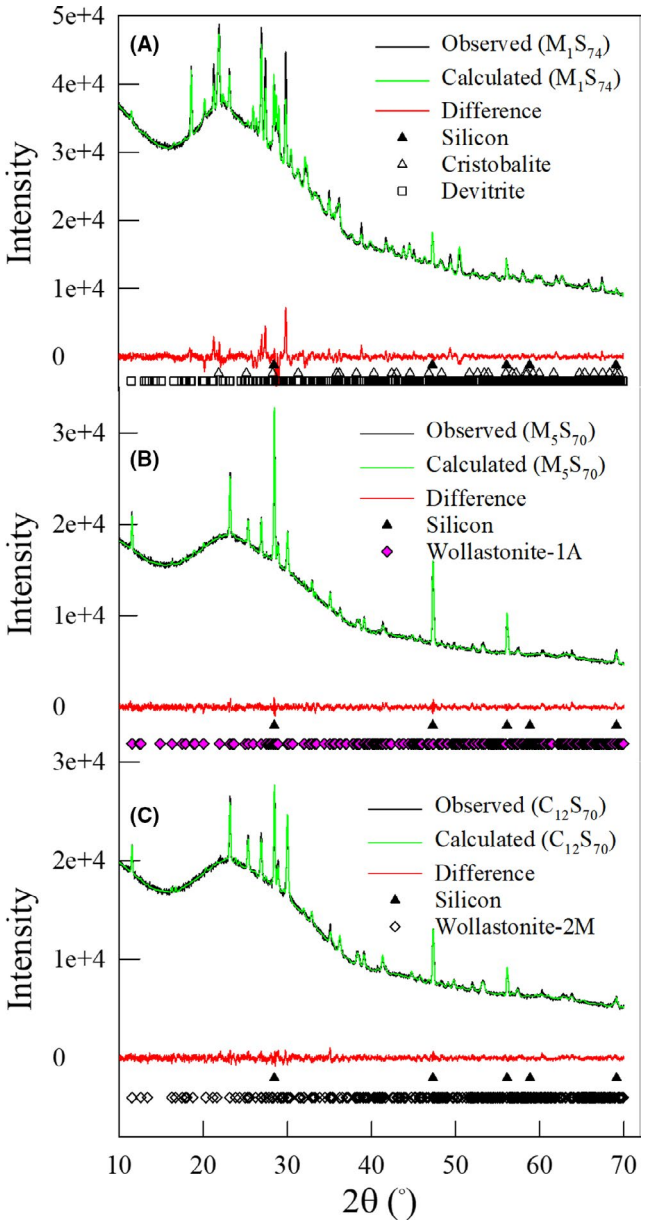


**FIGURE 3** Example of Rietveld difference plots from X'Pert XRD data (Cu$K\alpha$ X-rays) of various glasses with relatively larger bulk crystal fractions (A) $M_1S_{74}$, (B) $M_5S_{70}$, and (C) $C_{12}S_{70}$ glasses [Color figure can be viewed at wileyonlinelibrary.com]

vary within a narrow range; and the apparent discrepancy between the two sets of results can mainly be attributed to the temperatures at which the glasses were devitrified and, consequently, the respective crystallization rates. The devitrification temperature of the float glass compositions studied by Hrma et al[18] is much smaller than their actual liquidus temperatures ($\Delta T$ > 100°C), and these larger temperature differences likely gave rise to substantially higher crystallization rates and thus a greater crystalline fraction in their samples by comparison with those in this study. Figure 5A shows no significant variation in the fraction of glassy phase in the ASN glass series, based on overlapping uncertainties, although liquidus temperatures within this glass series vary

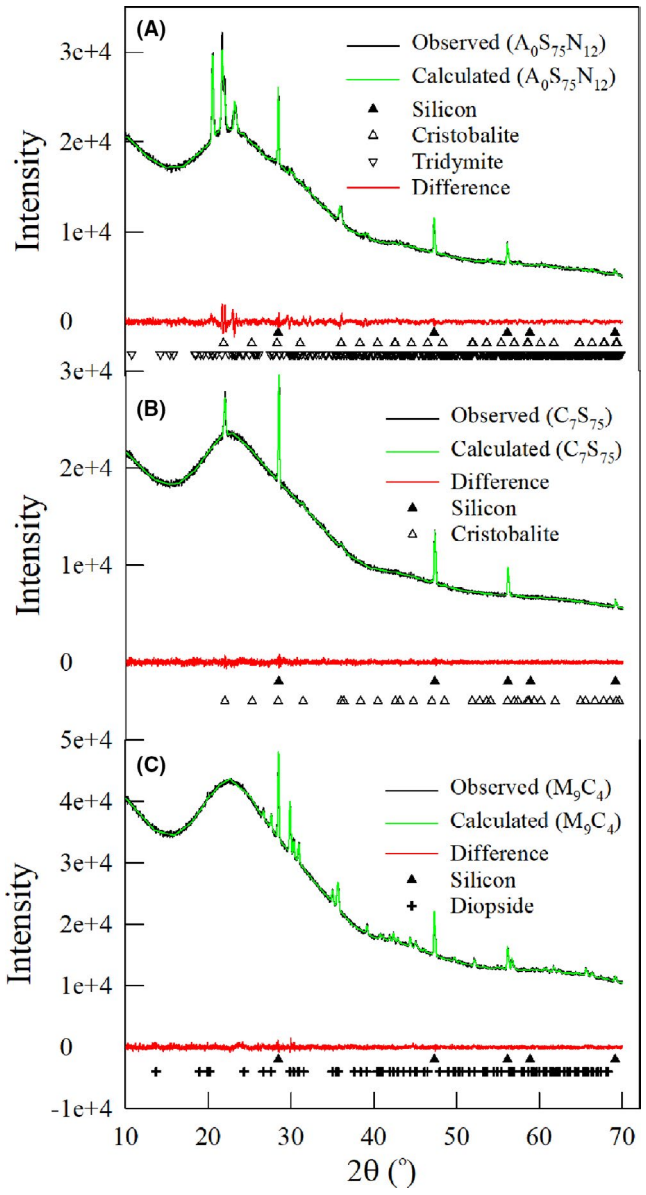


**FIGURE 4** Example of Rietveld difference plots from X'Pert XRD data (Cu*Kα* X-rays) of various glasses with relatively higher bulk amorphous phase fractions (A) $A_0S_{75}N_{12}$ and (B) $C_7S_{75}$ and (C) $M_9C_4$ glasses [Color figure can be viewed at wileyonlinelibrary.com]

within a wide range. In the MS glass series (Figure 5B), two local minima are observed as MgO replaces $SiO_2$, and one of the lowest glassy phase fractions observed in all glass series was obtained for the $M_1S_{74}$ glass with a primary phase field of devitrite—despite the fact that this glass has one of the lowest liquidus temperatures in the MS glass series. The goodness-of-fit of the Rietveld refinement for the $M_1S_{74}$ glass ($\chi^2 = 11.54$) is significantly poorer than those for the other MS series glasses (Table A2). The addition of diopside to the identified phases of devitrite and cristobalite slightly improves the goodness-of-fit ($\chi^2 = 9.03$) with a glassy phase fraction of 0.9176; and the $\chi^2$ can be further reduced to 7.947 with the additions of *β*-wollastonite and tridymite as fifth and sixth phases (including silicon standard), respectively. These relatively poor goodness-of-fit values might be caused by the overlapping diffraction peaks of minor but multiple crystalline phases present in the devitrified $M_1S_{74}$ glass. In comparison only devitrite and cristobalite are needed to evaluate the properties of $M_1S_{74}$ glass (Table 3). In the CS series (Figure 5C), the glassy phase fraction gradually decreases with replacing CaO for $SiO_2$, and reaches a minimum at ([MgO] + [CaO] / [$SiO_2$]) ≈ 0.22 before increasing again with further CaO additions.

Variation in the fraction of glassy phase across the MC glass series (Figure 5D) appears to be small and within the experimental uncertainties; however, a slight change in glassy phase fraction can be observed between the $M_5C_8$ and $M_7C_6$ glasses as the crystalline phase field moves from (wollastonite-*2 M* + cristobalite) to diopside. It is likely that the compositions lying between $M_5C_8$ and $M_7C_6$ glasses with around 4 wt% MgO would exhibit the lowest liquidus temperatures of all of the studied glasses, (Figure 1D and Figure 5D). Further to this, Kamita et al[53] found that the minimum in liquidus temperature was at ~4 wt% MgO in quinary $Na_2O$-MgO-CaO-$Al_2O_3$-$SiO_2$ glasses. These results clearly explain, and are consistent with, the presence of similar MgO levels in commercial float glass compositions, for which low liquidus temperatures and crystallization rates are ultimately desirable. It is likely that the primary phase field of such glass compositions might reside near the (wollastonite + cristobalite) phase fields, as was observed both here for the $M_5C_8$ glass, and in the literature for other commercial float glass compositions (e.g., Hrma et al[18]). In contrast to the MC glass series, a minimum in liquidus temperature values is not observed in the MgO-rich glasses of the MS glass series, whose MgO levels vary between 3.93 and 4.60 wt%. This indicates that the nonlinear variations in liquidus temperature cannot simply be attributed to the presence of certain amounts of MgO or to the type of the primary phase field transformation. The collated information from the phase equilibrium diagrams of the $Na_2O$-CaO-$SiO_2$ system and the isopleths of the $Na_2O$-CaO-$Al_2O_3$-$SiO_2$ system[51] at constant 5 and 10 mol % MgO reveals that the coordinates of most commercial glass compositions move toward the devitrite region through the wollastonite phase field and across the isotherms of lower liquidus temperatures, with increasing MgO/CaO ratios. This is likely reflected as a reduction in liquidus temperature until the diopside phase field is reached, and diopside phase field completely or partially replaces wollastonite and devitrite phase fields with relatively higher liquidus temperature isotherms, and this might explain the increase in liquidus temperatures with further MgO additions. On the other hand, increasing the MgO/$SiO_2$ ratio moves the glass composition toward the CaO-rich top corner along the higher liquidus temperature isotherms of the wollastonite phase field. The diopside phase field forms with higher liquidus temperature isotherms and

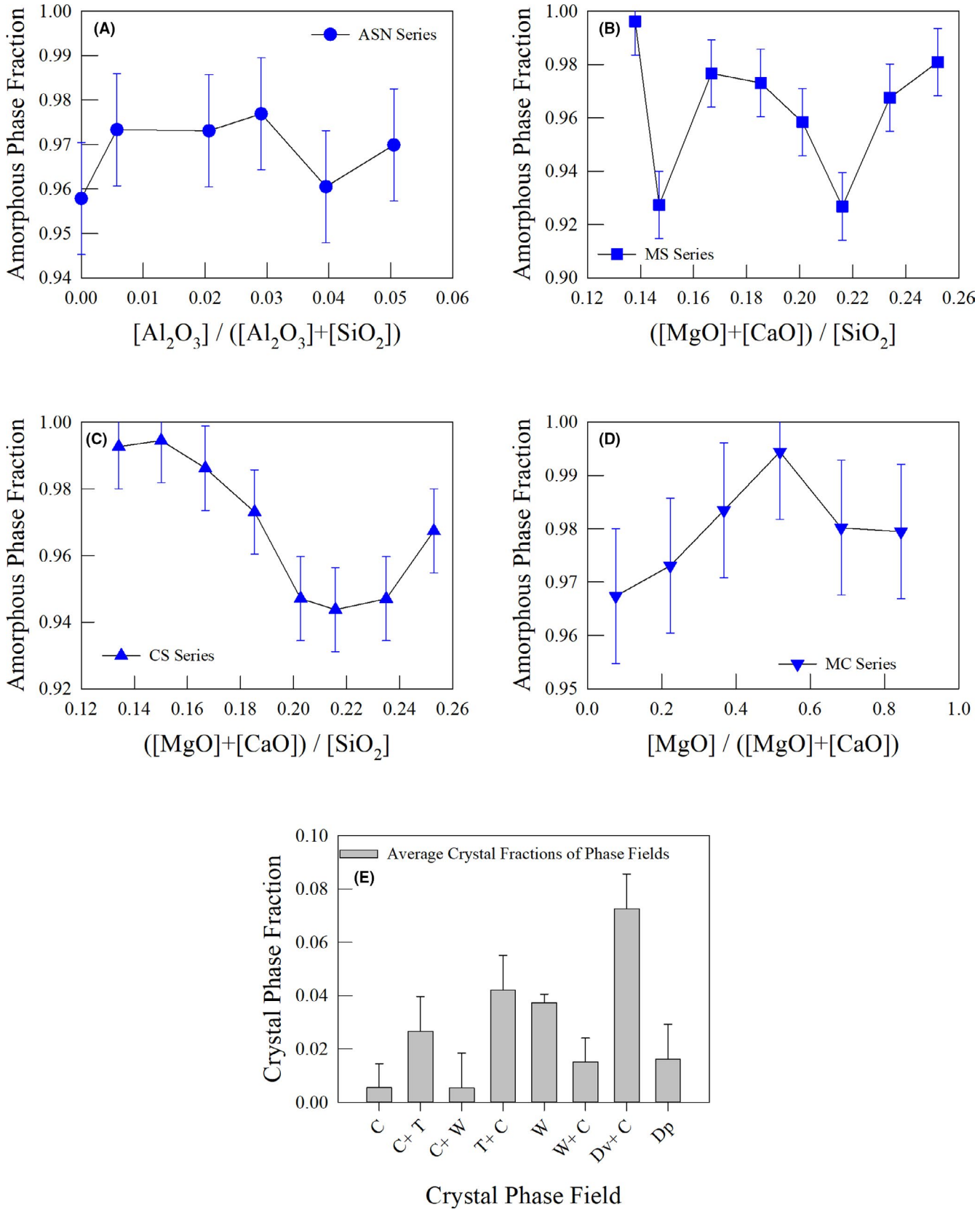


**FIGURE 5** Variation of glassy phase fractions in (A) ASN glass series, (B) MS glass series, (C) CS glass series, (D) MC glass series (± errors derived from the Rietveld refinement of two independent $A_{3.5}S_{68}N_{15.5}$ glass specimens); and (E) average crystal phase fractions of devitrified glasses classified by their single or mixed crystal phase fields. *C*, *T*, *Dv*, and *Dp* stand for cristobalite, tridymite, devitrite, and diopside, respectively. *W* indicates W-*2M* and/or W-*1A* phase fields. Single capital letter denotes the primary phase field, and the initial capital letter of the mixed phases stands for the primary phase field of mixed phase fields [Color figure can be viewed at wileyonlinelibrary.com]

**TABLE 3** Concentrations (wt %) of bulk crystal and amorphous phases in the ASN, MS, CS, and MC glass series calculated using the Rietveld refinement method

| | Experimental | | | | | | |
|---|---|---|---|---|---|---|---|
| **Glass ID** | ***T*** | ***C*** | ***Dv*** | ***W-1A*** | ***W-2 M*** | ***Dp*** | **% Amorp.** |
| $A_0S_{75}N_{12}$ | 2.69 ± 0.03 | 1.52 ± 0.03 | | | | | 95.79 ± 0.04 |
| $A_{0.5}S_{74}N_{12.5}$ | 0.82 ± 0.02 | 1.85 ± 0.06 | | | | | 97.33 ± 0.06 |
| **$A_{1.5}S_{72}N_{13.5}$** | | | | | **2.69 ± 0.10** | | **97.31 ± 0.10** |
| $A_{2.5}S_{70}N_{14.5}$ | | | | 2.31 ± 0.10 | | | 97.69 ± 0.10 |
| $A_{3.5}S_{68}N_{15.5}$ | | | | 3.95 ± 0.14 | | | 96.05 ± 0.14 |
| $A_{4.5}S_{66}N_{16.5}$ | | | | 3.01 ± 0.09 | | | 96.99 ± 0.09 |
| $M_0S_{75}$ | | 0.38 ± 0.01 | | | | | 99.62 ± 0.01 |
| $M_1S_{74}$ | | 0.78 ± 0.04 | 6.49 ± 0.10 | | | | 92.74 ± 0.11 |
| $M_2S_{73}$ | | 0.32 ± 0.01 | | | 2.01 ± 0.07 | | 97.67 ± 0.07 |
| **$M_3S_{72}$** | | | | | **2.69 ± 0.10** | | **97.31 ± 0.10** |
| $M_4S_{71}$ | | | | 4.17 ± 0.13 | | | 95.83 ± 0.13 |
| $M_5S_{70}$ | | | | 7.32 ± 0.22 | | | 92.68 ± 0.22 |
| $M_6S_{69}$ | | | | | 3.25 ± 0.09 | | 96.75 ± 0.09 |
| $M_7S_{68}$ | | | | | | 1.91 ± 0.06 | 98.09 ± 0.06 |
| $C_7S_{75}$ | | 0.73 ± 0.04 | | | | | 99.27 ± 0.04 |
| $C_8S_{74}$ | | 0.29 ± 0.01 | | 0.26 ± 0.03 | | | 99.45 ± 0.03 |
| $C_9S_{73}$ | | 0.12 ± 0.01 | | 1.26 ± 0.03 | | | 98.62 ± 0.03 |
| **$C_{10}S_{72}$** | | | | | **2.69 ± 0.10** | | **97.31 ± 0.10** |
| $C_{11}S_{71}$ | | | | 5.29 ± 0.15 | | | 94.71 ± 0.15 |
| $C_{12}S_{70}$ | | | | | 5.62 ± 0.11 | | 94.38 ± 0.11 |
| $C_{13}S_{69}$ | | | | 5.30 ± 0.15 | | | 94.70 ± 0.15 |
| $C_{14}S_{68}$ | | | | 3.26 ± 0.07 | | | 96.74 ± 0.07 |
| $M_1C_{12}$ | | | | 3.26 ± 0.06 | | | 96.74 ± 0.06 |
| **$M_3C_{10}$** | | | | | **2.69 ± 0.10** | | **97.31 ± 0.10** |
| $M_5C_8$ | | 0.33 ± 0.01 | | | 1.32 ± 0.04 | | 98.35 ± 0.04 |
| $M_7C_6$ | | | | | | 0.56 ± 0.05 | 99.44 ± 0.05 |
| $M_9C_4$ | | | | | | 1.98 ± 0.05 | 98.02 ± 0.05 |
| $M_{11}C_2$ | | | | | | 2.05 ± 0.05 | 97.95 ± 0.05 |

Errors are also given for the measured concentrations of primary and/or secondary phase fields of each glass series. Goodness of fit and unit cell parameters obtained from the X-Ray powder diffraction patterns of the glasses are presented in Appendix A. For reader convenience, base glass composition is denoted by $A_{1.5}S_{72}N_{13.5}$, $M_3S_{72}$, $C_{10}S_{72}$, and $M_3C_{10}$ in the four glass series (highlighted in bold in the table).

Error in % amorphous phase can be defined as follows: $= \sqrt{\left[(\delta T)^2 + (\delta C)^2 + (\delta Dv)^2 + \left(\delta W_{1-A}\right)^2 + \left(\delta W_{2M}\right)^2 + (\delta Dp)^2\right]}$.

replaces the wollastonite phase fields and therefore replacing $SiO_2$ by MgO tends to progressively increase the liquidus temperature of quinary soda-lime-silica glasses. Our $M_6S_{69}$ and $M_7S_{68}$ glasses resemble a representative commercial float glasses in chemical composition (72.6·$SiO_2$-13.5·$Na_2O$-8.4·CaO-4.4·MgO-0.5·$Al_2O_3$ in wt%, and $SO_3$, $K_2O$ and $TiO_2$ are 0.2 wt%, respectively; and $Fe_2O_3$ is 0.1 wt%),[54] and these glasses contain similar CaO, MgO, and $Na_2O$ levels (Table 1). Crystallization properties of representative commercial float glasses were discussed by Beerkens and Conradt[54]; with $\beta$-wollastonite found to be the primary phase field, and diopside can coexist as a secondary phase field just below the liquidus temperature. It appears that wollastonite is the primary phase field of $M_6S_{69}$ and the commercial float glass although the latter contains higher $SiO_2$ and lower $Al_2O_3$ than $M_6S_{69}$ and $M_7S_{68}$ glasses (Table 2); and increasing the MgO to $SiO_2$ ratio shifts the primary phase field from wollastonite to diopside in our $M_7S_{68}$ glass.

Swift[14] investigated the crystallization behavior of soda-lime-silica glasses by varying the MgO/CaO ratio on a weight basis, and observed a minimum rate of crystallization at ~6 wt% MgO as the primary phase field changes from devitrite to diopside. Backman et al[55] found that devitrite crystals were the fastest-growing, regardless of being primary,

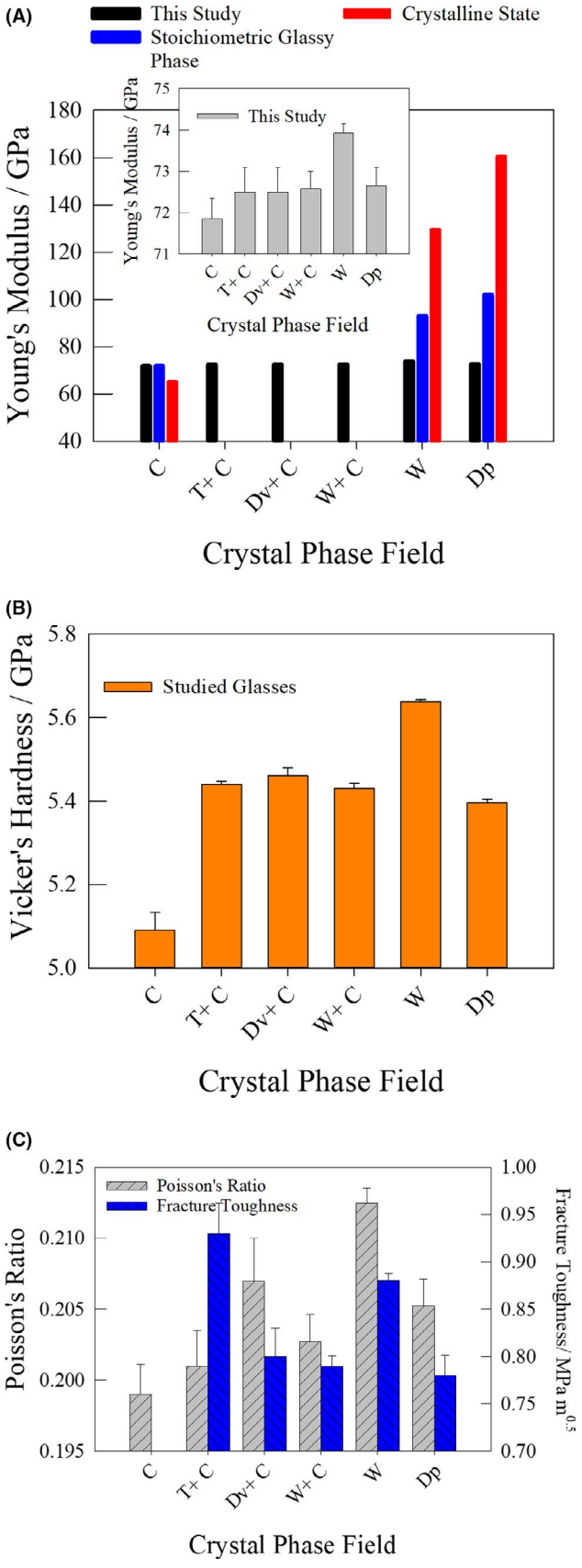


**FIGURE 6** (A) Young's moduli of stoichiometric glassy states of different phase fields from Phillips et al[59]; Young's moduli of crystalline states of low-cristobalite from Pabst and Gregorová,[57] wollastonite from Lin et al,[60] diopside from Aleksandrov et al[61]; and average Young's moduli of studied soda-lime-silica glasses based on their crystal phase field, (B) average Vickers hardness of soda-lime-silica glasses based on crystal phase field, (C) Measured average Poisson's ratio and fracture toughness values of soda-lime-silica glasses respect to their crystal phase fields [Color figure can be viewed at wileyonlinelibrary.com]

secondary or ternary phases. Surface crystallization studies by Zanotto[56] showed that the average number of crystals grown per unit area of float glass is the largest for devitrite (300–3000 $mm^{-2}$); and the lowest for tridymite (10 $mm^{-2}$), and in between for diopside (50 $mm^{-2}$). The results of the present work are consistent with all of the above literature, and complement the earlier work. Figure 5E summarizes the average crystal fractions of the studied soda-lime-silica glasses in terms of primary crystal phase field, and demonstrates that the rate of bulk crystallization of these glasses would significantly decrease when the primary phase field moves from devitrite to diopside. The highest rates of bulk crystallization are observed for the devitrite, tridymite, and wollastonite primary crystalline phase fields.

## 4.3 | Measured mechanical properties

Figure 6A shows the measured variations in average Young's moduli of glassy and crystalline states of corresponding crystal phase fields. Variation in average Young's moduli of soda-lime-silica glasses as a function of crystal phase field appears to be insignificant relative to the observed dramatic changes in stoichiometric glassy and crystalline state counterparts. However, for local soda-lime-silica glass quaternaries, soda-lime-silica glasses with wollastonite and cristobalite phase fields exhibit the highest and lowest average Young's moduli, respectively; moduli tend to remain constant for soda-lime-silica glasses with other remaining crystalline phase fields, and their average values range between those measured for the cristobalite and wollastonite phase fields. The Young's modulus of the stoichiometric glassy phase of $SiO_2$ is 72.0 GPa which is very close to that of soda-lime-silica glasses of the cristobalite phase field (71.9 GPa). However, the Young's modulus of the form of low-cristobalite polymorph is 65.2 GPa (from Pabst and Gregorová[57]), which is significantly lower than the corresponding glassy states. The difference between Young's moduli of stoichiometric wollastonite glass and soda-lime-silica glass within the wollastonite primary phase field grows significantly larger, and it reaches the largest value between stoichiometric diopside glass and its soda-lime-silica glass counterpart. Furthermore, as is seen in Figure 6A, variation of Young's modulus in these minerals with respect to the type of crystal phase field, bears similarities to the stoichiometric glassy phases and decreases in the order of primary crystal phase field of diopside >wollastonite

**TABLE 4** Measured physical and mechanical properties of the glasses studied here

| Glass ID | Density/ Mg m$^{-3}$ | Mechanical Properties | | | | |
|---|---|---|---|---|---|---|
| | | Young's Modulus/ GPa | Poisson's Ratio | Vicker's Hardness/ GPa | Fracture Tougness/ MPa m$^{0.5}$ | Britleness/ $\mu$m$^{-1/2}$ |
| $A_0S_{75}N_{12}$ | 2.462 ± 0.002 | 72.4 ± 0.76 | 0.203 ± 0.003 | 5.40 ± 0.01 | 0.96 ± 0.05 | 5.63 ± 0.05 |
| $A_{0.5}S_{74}N_{12.5}$ | 2.469 ± 0.001 | 72.6 ± 0.93 | 0.199 ± 0.004 | 5.48 ± 0.01 | 0.90 ± 0.04 | 6.09 ± 0.04 |
| $A_{1.5}S_{72}N_{13.5}$ | 2.485 ± 0.001 | 73.3 ± 0.47 | 0.211 ± 0.002 | 5.63 ± 0.02 | 0.82 ± 0.01 | 6.87 ± 0.01 |
| $A_{2.5}S_{70}N_{14.5}$ | 2.497 ± 0.001 | 73.3 ± 0.95 | 0.209 ± 0.004 | 5.54 ± 0.01 | 0.86 ± 0.03 | 6.44 ± 0.03 |
| $A_{3.5}S_{68}N_{15.5}$ | 2.506 ± 0.002 | 73.4 ± 0.94 | 0.211 ± 0.004 | 5.62 ± 0.01 | 0.90 ± 0.02 | 6.24 ± 0.02 |
| $A_{4.5}S_{66}N_{16.5}$ | 2.519 ± 0.001 | 73.5 ± 0.88 | 0.214 ± 0.004 | 5.54 ± 0.01 | 0.91 ± 0.03 | 6.09 ± 0.03 |
| $M_0S_{75}$ | 2.465 ± 0.001 | 71.9 ± 0.68 | 0.201 ± 0.003 | 5.11 ± 0.07 | - | - |
| $M_1S_{74}$ | 2.475 ± 0.001 | 72.5 ± 0.59 | 0.207 ± 0.003 | 5.46 ± 0.02 | 0.80 ± 0.03 | 6.83 ± 0.04 |
| $M_2S_{73}$ | 2.480 ± 0.001 | 72.5 ± 0.88 | 0.204 ± 0.004 | 5.52 ± 0.03 | 0.82 ± 0.02 | 6.73 ± 0.02 |
| $M_3S_{72}$ | 2.485 ± 0.001 | 73.3 ± 0.47 | 0.211 ± 0.002 | 5.63 ± 0.02 | 0.82 ± 0.01 | 6.87 ± 0.01 |
| $M_4S_{71}$ | 2.496 ± 0.001 | 73.6 ± 0.62 | 0.214 ± 0.003 | 5.64 ± 0.02 | 0.89 ± 0.03 | 6.34 ± 0.03 |
| $M_5S_{70}$ | 2.504 ± 0.001 | 74.0 ± 0.70 | 0.217 ± 0.003 | 5.72 ± 0.01 | 0.85 ± 0.03 | 6.73 ± 0.04 |
| $M_6S_{69}$ | 2.513 ± 0.001 | 74.0 ± 0.88 | 0.213 ± 0.004 | 5.73 ± 0.02 | 0.88 ± 0.01 | 6.51 ± 0.01 |
| $M_7S_{68}$ | 2.520 ± 0.001 | 75.7 ± 0.74 | 0.214 ± 0.003 | 5.96 ± 0.02 | 0.80 ± 0.03 | 7.45 ± 0.04 |
| $C_7S_{75}$ | 2.445 ± 0.001 | 71.8 ± 0.70 | 0.197 ± 0.003 | 5.07 ± 0.05 | - | - |
| $C_8S_{74}$ | 2.462 ± 0.001 | 72.0 ± 0.78 | 0.199 ± 0.003 | 5.37 ± 0.03 | 0.78 ± 0.02 | 6.88 ± 0.03 |
| $C_9S_{73}$ | 2.474 ± 0.001 | 72.7 ± 0.81 | 0.201 ± 0.004 | 5.50 ± 0.02 | 0.83 ± 0.03 | 6.63 ± 0.04 |
| $C_{10}S_{72}$ | 2.485 ± 0.001 | 73.3 ± 0.47 | 0.211 ± 0.002 | 5.63 ± 0.02 | 0.82 ± 0.01 | 6.87 ± 0.01 |
| $C_{11}S_{71}$ | 2.504 ± 0.001 | 74.0 ± 0.72 | 0.213 ± 0.003 | 5.65 ± 0.02 | 0.89 ± 0.03 | 6.35 ± 0.03 |
| $C_{12}S_{70}$ | 2.508 ± 0.001 | 73.8 ± 0.57 | 0.217 ± 0.003 | 5.69 ± 0.02 | 0.90 ± 0.02 | 6.32 ± 0.02 |
| $C_{13}S_{69}$ | 2.529 ± 0.001 | 74.9 ± 1.08 | 0.207 ± 0.005 | 5.69 ± 0.03 | 0.86 ± 0.03 | 6.62 ± 0.04 |
| $C_{14}S_{68}$ | 2.542 ± 0.001 | 75.6 ± 0.98 | 0.213 ± 0.004 | 5.81 ± 0.01 | 0.95 ± 0.02 | 6.12 ± 0.02 |
| $M_1C_{12}$ | 2.502 ± 0.001 | 73.7 ± 0.60 | 0.211 ± 0.003 | 5.39 ± 0.01 | 0.86 ± 0.03 | 6.27 ± 0.03 |
| $M_3C_{10}$ | 2.485 ± 0.001 | 73.3 ± 0.47 | 0.211 ± 0.002 | 5.63 ± 0.09 | 0.82 ± 0.01 | 6.87 ± 0.02 |
| $M_5C_8$ | 2.469 ± 0.001 | 73.1 ± 0.92 | 0.207 ± 0.004 | 5.33 ± 0.01 | 0.73 ± 0.01 | 7.30 ± 0.01 |
| $M_7C_6$ | 2.457 ± 0.001 | 72.8 ± 0.93 | 0.199 ± 0.004 | 5.25 ± 0.02 | 0.78 ± 0.05 | 6.73 ± 0.06 |
| $M_9C_4$ | 2.446 ± 0.003 | 71.4 ± 0.93 | 0.205 ± 0.004 | 5.21 ± 0.01 | 0.76 ± 0.02 | 6.86 ± 0.03 |
| $M_{11}C_2$ | 2.433 ± 0.001 | 70.7 ± 0.92 | 0.203 ± 0.004 | 5.16 ± 0.02 | 0.78 ± 0.06 | 6.62 ± 0.08 |

The most of the data presented in the table taken from Kilinc and Hand[6] and Kilinc.[64] Standard deviation was used to estimate the errors in Kilinc and Hand[6]. Here $SE = SD/\sqrt{N}$ was used to calculate the error of mean of measured properties where *SE*, *SD*, and *N* are standard error, standard deviation, and the number of measurement in a group, respectively.

> silica. These mineral phases exhibit the largest Young's moduli values when compared to their stoichiometric glassy or soda-lime-silica glass counterparts.

As shown in Figure 6B, soda-lime-silica glasses within the cristobalite and wollastonite primary phase fields exhibit the lowest and the highest average Vicker's hardness ($H_v$) values, respectively. The soda-lime-silica glasses within the cristobalite phase field show disproportionately low $H_v$ compared with the glasses within other primary phase fields, and mixed phases of cristobalite with tridymite improve the hardness of the soda-lime-silica glasses in silica phase fields. Glasses within other phase fields exhibit similar average hardness values and vary between the lowest and the highest values for cristobalite and wollastonite phase fields, respectively. These findings are consistent with the results of Georoff and Babcock,[9] who found that the Knoop hardness of soda-lime-silica glasses (compositions from Morey's[10] $SiO_2$-$Na_2O$-CaO phase diagram) decreases in the order $\beta$–wollastonite >devitrite = tridymite > $Na_2O{\cdot}2SiO_2$ when compared in terms of crystal phase field.

Soda-lime-silica glasses within the $SiO_2$ primary phase fields (*T + C or C + T*) exhibit the highest fracture toughness values (Table 4), and this is followed by soda-lime-silica glasses within the wollastonite phase field. Glasses within the diopside phase field, or located near other phase boundaries (*Dv + C* and *W + C*), exhibit the lowest fracture toughness

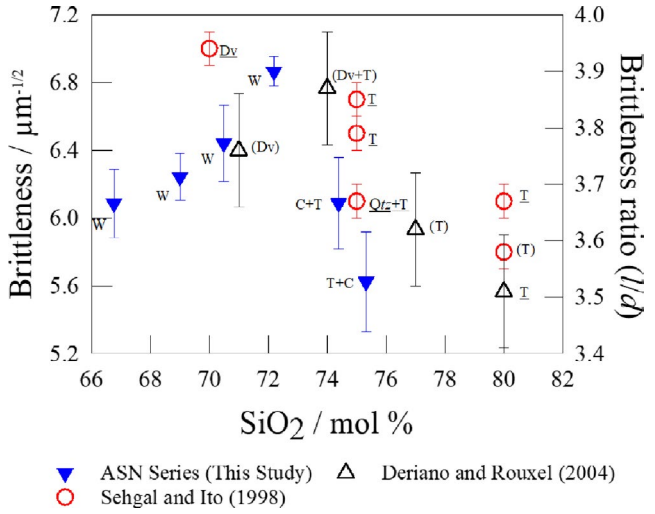


**FIGURE 7** Variation in brittleness and brittleness ratio (*l*/*d*) values of various glass series with molar $SiO_2$ concentration. *C*, *T*, *Qtz*, and *Dv* indicate cristobalite, tridymite, quartz, and devitrite phase fields, respectively. *W* stands for wollastonite-*1A* in ASN glass series except the base glass ($A_{1.5}S_{72}N_{13.5}$) for which *W* denotes wollastonite-*2M* [Color figure can be viewed at wileyonlinelibrary.com]

values (Figure 6C). Although the Young's moduli ($E$) and plane strain moduli $E' = E / (1 - \upsilon^2)$ of the studied soda-lime-silica glasses vary within a narrow range (Figure 6A), the measured fracture toughness values vary considerably with composition and increase by ~30% relative to the lowest fracture toughness across all studied glass compositions. Given it can be shown that

$$K_c = \sqrt{2E'\gamma} \tag{14}$$

where $\gamma$ is the fracture surface energy[58] and this implies the surface energy may be notably different for the glasses corresponding to the different phase fields.

The significant role of Poisson's ratio on indentation cracking of different types of glass was previously revealed by Rouxel,[1] and our previously published data[6] also showed that the silicate glasses that exhibit semi-resilient behavior ($0.20 \leq \nu \leq 0.25$) have greater fracture toughness values that tend to increase with increasing Poisson's ratio. However, the glasses of the ASN series studied here, within the $SiO_2$ phase field, do not behave in a similar manner and exhibit the highest fracture toughness values with the lowest Poisson's ratio values (Figure 6C).

Figure 7 compares the brittleness data as a function of molar $SiO_2$ content for the ASN glass series with data published by Sehgal and Ito[4] and Deriano and Rouxel.[7] Sehgal and Ito[62] attempted to explain the behavior of brittleness of silicate glasses in terms of their being anomalous or normal glasses. They observed that the brittleness decreases with decreasing density or increasing higher molar volume within the normal glass systems.[4] Anomalous and normal glasses

**TABLE 5** Calculated properties of glasses studied here. Error in molar volume, $V_M$, (see Equation 2) can be calculated by using: $\frac{\delta V_M}{V_M} = \sqrt{\left[\frac{(\delta(\sum J_i M_i))}{(\sum J_i M_i)}\right]^2 + \left[\frac{\delta\rho}{\rho}\right]^2}$

| Glass ID | Calculated Glass Properties | |
|---|---|---|
| | Molar Volume/ $cm^3$/mol | Atomic Packing Density |
| $A_0S_{75}N_{12}$ | 24.1 ± 0.2 | 0.495 |
| $A_{0.5}S_{74}N_{12.5}$ | 24.1 ± 0.2 | 0.496 |
| **$A_{1.5}S_{72}N_{13.5}$** | **24.1 ± 0.2** | **0.497** |
| $A_{2.5}S_{70}N_{14.5}$ | 24.1 ± 0.2 | 0.499 |
| $A_{3.5}S_{68}N_{15.5}$ | 24.2 ± 0.2 | 0.499 |
| $A_{4.5}S_{66}N_{16.5}$ | 24.2 ± 0.2 | 0.501 |
| $M_0S_{75}$ | 24.6 ± 0.2 | 0.495 |
| $M_1S_{74}$ | 24.4 ± 0.2 | 0.496 |
| $M_2S_{73}$ | 24.3 ± 0.2 | 0.497 |
| **$M_3S_{72}$** | **24.1 ± 0.2** | **0.497** |
| $M_4S_{71}$ | 24.0 ± 0.2 | 0.499 |
| $M_5S_{70}$ | 23.8 ± 0.2 | 0.500 |
| $M_6S_{69}$ | 23.7 ± 0.2 | 0.501 |
| $M_7S_{68}$ | 23.5 ± 0.2 | 0.502 |
| $C_7S_{75}$ | 24.6 ± 0.2 | 0.492 |
| $C_8S_{74}$ | 24.4 ± 0.2 | 0.494 |
| $C_9S_{73}$ | 24.3 ± 0.2 | 0.496 |
| **$C_{10}S_{72}$** | **24.1 ± 0.2** | **0.497** |
| $C_{11}S_{71}$ | 23.9 ± 0.2 | 0.500 |
| $C_{12}S_{70}$ | 23.9 ± 0.2 | 0.500 |
| $C_{13}S_{69}$ | 23.7 ± 0.2 | 0.504 |
| $C_{14}S_{68}$ | 23.5 ± 0.2 | 0.505 |
| $M_1C_{12}$ | 24.1 ± 0.2 | 0.500 |
| **$M_3C_{10}$** | **24.1 ± 0.2** | **0.497** |
| $M_5C_8$ | 24.1 ± 0.2 | 0.495 |
| $M_7C_6$ | 24.1 ± 0.2 | 0.493 |
| $M_9C_4$ | 24.1 ± 0.2 | 0.491 |
| $M_{11}C_2$ | 24.1 ± 0.2 | 0.489 |

For reader convenience base glass composition is denoted by different glass codes as $A_{1.5}S_{72}N_{13.5}$, $M_3S_{72}$, $C_{10}S_{72}$, and $M_3C_{10}$ in four glass series (highlighted in bold in the table).

differ from each other according to their cracking patterns under sharp contact loading, and median/radial and Hertzian-like cone cracks are the distinctive crack characteristics of normal and anomalous glasses, respectively.[63] The glasses studied here are deemed to be normal glasses based on the indentation studies.[64] However, the brittleness values do not correlate with either the density values. In fact, the molar volumes of the ASN glasses remain nearly constant (Table 5), whereas the brittleness exhibits a nonlinear variation across the compositional range. Further to this, atomic packing density (Table 5) shows a linear relationship with composition in

the different studied glass series ($R^2$ = 0.99, 0.97, 0.99 and 0.99 for ASN, MS, CS, and MC glass series, respectively); however, $C_g$ is far from explaining the nonlinear variation of brittleness in ASN glass series or disproportionally low hardness values observed in glasses within cristobalite phase field (Figure 6B). A similar conclusion can be reached from the work of Ying Shi et al[65] in which the Vicker's hardness of $x$CaO·$x$Al$_2$O$_3$·(1-2$x$)SiO$_2$ glasses exhibits nonlinear variation with SiO$_2$ (mol %) content. It is therefore concluded that the density, molar volume and/or packing density of silicate and aluminosilicate glasses do not suffice to explain the variations in mechanical properties of the silicate glasses measured here.

Brittleness of glasses in the ASN glass series within the wollastonite primary phase field increases with increasing SiO$_2$ content up to ~72 mol% and thereafter decreases with further SiO$_2$ additions as the primary phase field transforms from wollastonite to a mixed cristobalite and tridymite phase field. Similar nonlinear variation of the ratio of the indentation crack length (*l*) to the average diagonal length (*d*) can be observed in results for the SiO$_2$-CaO-Na$_2$O glasses of Deriano and Rouxel[7] (Table 6) as the primary phase field transforms from devitrite to tridymite. It appears that the findings of Sehgal and Ito[4] (Table 6) complement these observations, and their low brittleness SiO$_2$-CaO-Na$_2$O glasses mainly fall in the tridymite phase field, and the indentation brittleness decreases with increasing SiO$_2$ content. It can be concluded that the lowest brittleness values can be observed for the SiO$_2$-Na$_2$O-CaO glasses within the silica phase fields at ~80 mol% SiO$_2$, but SiO$_2$-Na$_2$O-CaO-MgO-Al$_2$O$_3$ quaternaries can also exhibit these low brittleness values at lower SiO$_2$ contents of ~75 mol%. These findings suggest that the nonlinear compositional dependence of brittleness can be linked to the transformations associated with primary phase field changes.

Unlike the observation of Jialiang,[66] the information acquired from IR absorption spectra of the four glass series studied here, or previously published $^{29}$Si MAS-NMR data for the MS and CS glass series, do not reveal any structural footprint that could be attributed to the shift of crystal phase field.[6,64] Further to this, our previously published work[6] showed that the substitution of CaO or MgO for SiO$_2$ depolymerizes glass network, as opposed to the polymerization of glasses with increasing MgO/CaO ratios; and the polymerization index of the ASN glass series decreases slightly with increasing [Al$_2$O$_3$+Na$_2$O]/[SiO$_2$] ratios.[64]

On the other hand, the lower-frequency region of the Raman spectra of the studied glasses provides fine structural features, and stretching of Si-O bonds in five, six member and larger rings give rise to the long tail between ~250 and 480 cm$^{-1}$ in silicate glasses.[30] This lower-frequency Raman band is also defined as *R* band and comprises the contributions from higher membered rings (greater than three and four-membered rings).[67] Figure 8A shows that increasing CaO/SiO$_2$ and MgO/SiO$_2$ ratios give rise to significant intensity reduction in the long tail of the low-frequency band ($B_1$), whereas the replacement of CaO by MgO considerably increases the intensities of the $B_1$ bands. These findings suggest that replacing CaO or MgO for SiO$_2$ significantly reduces the number of high-membered rings in the network by creating smaller membered rings, and this is more pronounced in the case of substituting CaO for SiO$_2$. The lower-frequency region of the Raman spectra for the MC series glasses indicates that Mg$^{2+}$ acts differently when it is substituted for Ca$^{2+}$, and increasing MgO/CaO ratios considerably increase the intensity of the $B_1$ band, which suggests an increasing number of high-membered rings in the structure of the higher MgO glasses.

**TABLE 6** Properties of glasses which are taken from Sehgal and Ito[4] and Deriano and Rouxel[7]

| References | Glass No | Predicted Crystal Phase Fields, *from* Morey's phase diagram[10] | Na$_2$O | CaO | SiO$_2$ | Brittleness/ $\mu$m$^{-1/2}$ |
|---|---|---|---|---|---|---|
| Sehgal and Ito[4] | 1 | T | 15 | 5 | 80 | 5.8 ± 0.1 |
| | 2 | T | 10 | 10 | 80 | 6.1 ± 0.1 |
| | 3 | Qtz +T | 20 | 5 | 75 | 6.1 ± 0.1 |
| | 4 | T | 15 | 10 | 75 | 6.5 ± 0.1 |
| | 5 | T | 10 | 15 | 75 | 6.7 ± 0.1 |
| | 6 | Dv | 20 | 10 | 70 | 7.0 ± 0.1 |
| **References** | **Glass No** | **Predicted Crystal Phase Fields, *from* Morey's phase diagram[10]** | **Na$_2$O** | **CaO** | **SiO$_2$** | **Brittleness ratio (*l*/*d*)** |
| Deriano and Rouxel[7] | 7 | Dv | 18.09 | 10.76 | 71.15 | 3.76 ± 0.1 |
| | 8 | Dv +T | 16.23 | 9.63 | 74.14 | 3.87 ± 0.1 |
| | 9 | T | 14.36 | 8.51 | 77.13 | 3.62 ± 0.1 |
| | 10 | T | 12.5 | 7.38 | 80.12 | 3.51 ± 0.1 |

Glass compositions are presented in mol %.

**TABLE 7** Modeled liquidus viscosity, melting, annealing temperature, and working range of the studied glasses by a global statistical viscosity model of Fluegel[20]

| Glass ID | Liquidus Viscosity/ log$\eta$(dPa-s) | Melting temperature at Log$\eta$ = 2/ dPa-s | $T_{3.7}$/°C | $T_{3.7} - T_{liq}$/°C | Annealing temperature/°C at Log$\eta$ = 13.3/ dPa-s |
|---|---|---|---|---|---|
| $A_0S_{75}N_{12}$ | 3.20 | 1494.0 | 1104.2 | −86.8 | 558.7 |
| $A_{0.5}S_{74}N_{12.5}$ | 3.60 | 1486.4 | 1097.8 | −16.2 | 557.2 |
| $A_{1.5}S_{72}N_{13.5}$ | 3.99 | 1474.8 | 1087.7 | 42.7 | 556.7 |
| $A_{2.5}S_{70}N_{14.5}$ | 3.99 | 1455.0 | 1070.5 | 42.6 | 551.6 |
| $A_{3.5}S_{68}N_{15.5}$ | 3.87 | 1445.9 | 1061.6 | 25.6 | 550.2 |
| $A_{4.5}S_{66}N_{16.5}$ | 3.73 | 1425.2 | 1044.0 | 5.0 | 548.0 |
| $M_0S_{75}$ | 4.22 | 1493.2 | 1096.7 | 74.7 | 556.8 |
| $M_1S_{74}$ | 4.46 | 1486.3 | 1091.6 | 104.6 | 552.9 |
| $M_2S_{73}$ | 4.15 | 1476.2 | 1086.4 | 64.1 | 554.4 |
| $M_3S_{72}$ | 3.99 | 1474.8 | 1087.7 | 42.7 | 556.7 |
| $M_4S_{71}$ | 4.00 | 1454.5 | 1073.0 | 42.7 | 552.2 |
| $M_5S_{70}$ | 3.80 | 1441.3 | 1063.6 | 14.3 | 548.7 |
| $M_6S_{69}$ | 3.83 | 1440.4 | 1065.2 | 19.2 | 550.7 |
| $M_7S_{68}$ | 3.71 | 1431.1 | 1059.6 | 1.6 | 549.6 |
| $C_7S_{75}$ | 4.36 | 1527.2 | 1120.1 | 97.1 | 545.2 |
| $C_8S_{74}$ | 4.57 | 1494.4 | 1096.7 | 119.7 | 544.8 |
| $C_9S_{73}$ | 4.38 | 1488.3 | 1095.1 | 95.1 | 551.8 |
| $C_{10}S_{72}$ | 3.99 | 1474.8 | 1087.7 | 42.7 | 556.7 |
| $C_{11}S_{71}$ | 3.97 | 1454.8 | 1074.8 | 38.8 | 558.9 |
| $C_{12}S_{70}$ | 3.65 | 1440.4 | 1065.7 | −7.3 | 561.0 |
| $C_{13}S_{69}$ | 3.46 | 1422.7 | 1054.7 | −36.3 | 563.8 |
| $C_{14}S_{68}$ | 3.31 | 1407.5 | 1045.6 | −59.4 | 566.2 |
| $M_1C_{12}$ | 3.87 | 1448.8 | 1070.1 | 25.1 | 559.7 |
| $M_3C_{10}$ | 3.99 | 1474.8 | 1087.7 | 43.2 | 556.7 |
| $M_5C_8$ | 4.57 | 1485.8 | 1094.7 | 118.7 | 544.7 |
| $M_7C_6$ | 4.46 | 1505.9 | 1111.7 | 108.7 | 538.3 |
| $M_9C_4$ | 4.41 | 1517.6 | 1124.7 | 103.7 | 530.5 |
| $M_{11}C_2$ | 4.78 | 1527.7 | 1138.2 | 151.6 | 523.0 |

$T_{3.7}$ corresponds to the lowest processing temperature of glass melt at log ($\eta$/dPa-s) = 3.7. Liquidus viscosity was calculated using measured $T_{Liq}$ and VFT constants provided from Fluegel's viscosity model.

However, the intensity of the $B_2$ band, which is attributed to the existence of four ($D_1$ band from Hehlen and Neuville[67]) or three ($D_2$ band from Hehlen and Neuville[67]) membered rings[30] is disproportionately higher relative to the $B_1$ band in the $A_0S_{75}N_{12}$ and $A_{0.5}S_{74}N_{12.5}$ glasses studied here (Figure 8A-B), unlike in other glass series. This might indicate that in soda-lime-silica glasses in which $Al_2O_3$ is absent or at very low levels formation of smaller rings is promoted, which may lower brittleness owing to increased shear flow.[68] This could be an underlying reason for the improved brittleness in CaO-rich or low-$Al_2O_3$ glasses lying in the wollastonite and silica phase fields, respectively.

Glass technology has sought novel low melting soda-lime-silica glass compositions in order to optimize energy demand and carbon emissions, provided that the desired crystallization, viscosity, durability, and refractory compatibility properties of glass are attained.[19,37,40,69] On the other hand, brittleness is an important service property of container and flat glasses, and varies greatly by altering the balance of pre-existing oxides, thus the influence of compositional reformulations on brittleness should be evaluated. Although the brittleness is not simply the response variable of liquidus viscosity and melting temperature of glass, Figure 9A-B connects the measured brittleness values of various soda-lime-silica glasses with their liquidus viscosities and melting temperatures. The compositional ranges of the studied glasses are collectively much wider than that of commercial soda-lime-silica glasses, and therefore Figure 9A can be taken to

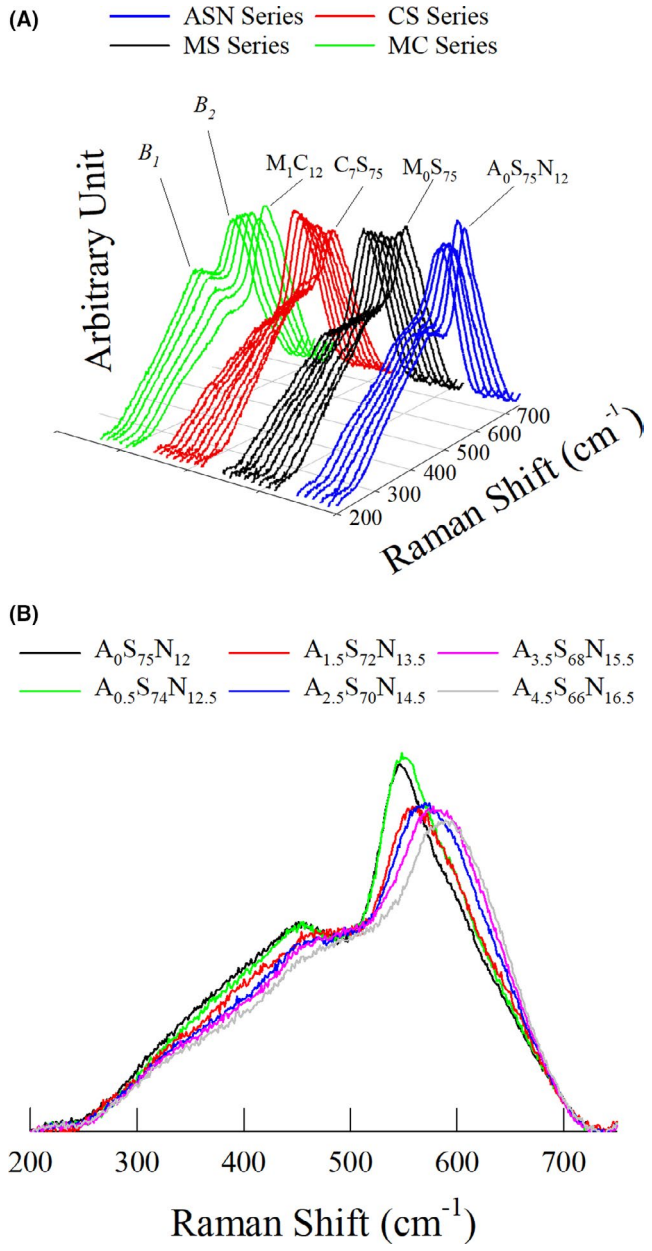


**FIGURE 8** (A) Low-frequency band of Raman spectra of ASN, MS, CS, and MC glass series, and $A_0S_{75}N_{12}$, $M_0S_{75}$, $C_7S_{75}$, and $M_1C_{12}$ glasses donate the first serial glass in ASN, MS, CS, and MC glass series, respectively. (B) The front view of the main low frequency Raman bands of ASN glass series [Color figure can be viewed at wileyonlinelibrary.com]

represent all possible extreme variations of these parameters with respect to each other, hence a simultaneous change in brittleness, liquidus viscosity, and melting temperature can be evaluated from a broad perspective. Figure 9B demonstrates that low brittleness values can be observed for the glasses within the wollastonite phase field in the lower melting temperature region (1450°C < $T_m$), and their liquidus viscosities (i.e., log ($\eta$/dPa-s) = 3 to 4) tend to be much lower than those of the glasses exhibiting high brittleness and high melting temperatures. On the other hand, glasses within the silica

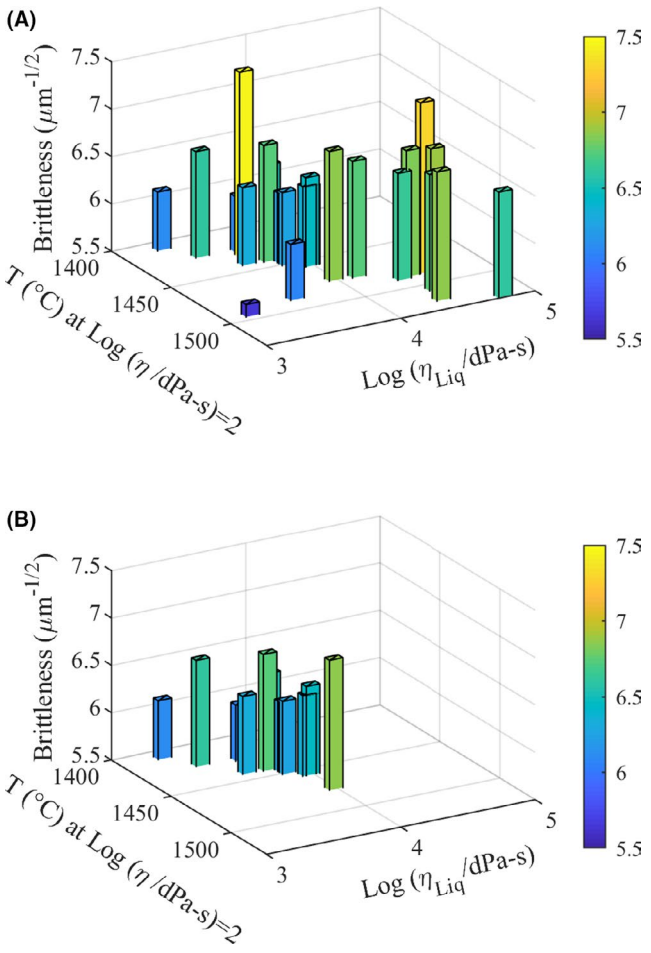


**FIGURE 9** (A) 3D Property plot of ASN, MS, CS, and MC glass series with the parameters of brittleness, liquidus viscosity, and melting temperature. (B) Glasses with primary phase field of wollastonite (*1-A or 2M*) from different glass series [Color figure can be viewed at wileyonlinelibrary.com]

phase fields (i.e., $A_0S_{75}N_{12}$ and $A_{0.5}S_{74}N_{12.5}$ glasses) exhibit the lowest brittleness values, with one of the lowest liquidus viscosities smaller than log ($\eta$/dPa-s) = 4 dPa-s (Table 4). However, these glasses have melting temperatures greater than 1450°C in all the glass series studied here. Moreover, the glasses that reside in the neighborhood of (wollastonite + silica) or diopside phase fields tend to exhibit relatively high melting temperatures (1450°C > $T_m$) with liquidus viscosities greater than log ($\eta$/dPa-s) = 4.

Glasses with low brittleness values appear to have lower viscosities at their liquidus temperatures; however, the glass melts with higher viscosities at their liquidus temperatures would be more desirable as these melts possess larger kinetic barriers to devitrification.[70] On the contrary, variation of bulk crystal fraction of the studied glasses with liquidus viscosity does not exhibit a clear relationship. Further to this, glass melts that are processed with lower temperatures than their liquidus temperatures could be more susceptible to devitrification[19,37]; particularly for stagnant or colored glass melts[71] that remain relatively cool due to poorer heat transfer through

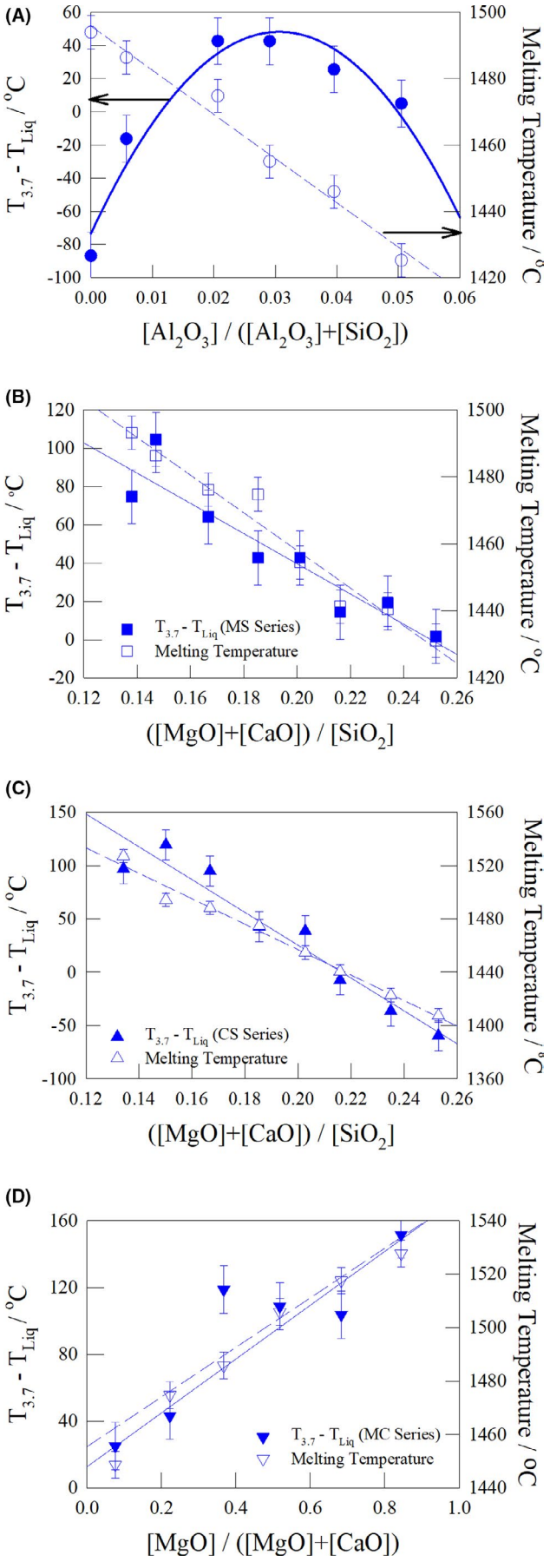


**FIGURE 10** Working range ($\Delta T = T_{3.7} - T_{Liq}$) and melting temperature of A) ASN, B) MS, C) CS, and D) MC glass series. Fluegel viscosity model's[20] sensitivity is 1.7 and 1.0°C for log ($\eta$/dPa-s) = 1.5 and 6.6, respectively. A maximum variation of ±5.0°C would be estimated for log ($\eta$/dPa-s) = 2. (Errors in $\Delta T$ can be calculated by using $\delta\Delta T = \sqrt{(\delta\Delta T_{3.7})^2 + (\delta T_{Liq})^2}$ where the $\delta\Delta T_{3.7} = 38$°C and $\delta TLiq = 10$°C are the errors associated with modeled temperature at log ($\eta$/dPa-s) = 3.7 and the measured liquidus temperature values, respectively [Color figure can be viewed at wileyonlinelibrary.com]

the melt, and this may lead to defects in the final product or even furnace failure in the event of excessive devitrification. Devitrification of glass melts can also be inhibited thermodynamically by increasing the temperature difference between corresponding processing temperatures and liquidus temperature. The $T_{3.7}$ can be regarded as the lowest processing temperatures of hollowware and float glasses at which the ideal viscosity ($10^{3.7}$ dPa-s)[37,40] of melt is attained for gob forming and inflow of melt to tin bath. Figure 10A-D and Table 7 show that $\Delta T = T_{3.7} - T_{Liq}$ and melting temperature of glasses decrease with increasing $MgO/SiO_2$ and $CaO/SiO_2$ molar ratios; but these variations are more pronounced in the case of $CaO/SiO_2$ substitution, and $\Delta T$ values move to negative values. Figure 10D also shows that increasing molar ratios of MgO/CaO gives rise to one of the highest melting temperatures as $\Delta T$ shifts to the largest positive values in all glass series. Figure 10A-D indicate that the relation between glass composition and $\Delta T$ or melting temperature would be linear for single oxide substitutions in MS, CS, and MC glass series. Similarly, melting temperatures of glasses in the ASN series tend to decrease linearly with an increasing ratio of $[Al_2O_3+Na_2O]/[SiO_2]$. However, $\Delta T$ values abruptly shift from strongly negative to positive, unlike in the other glass series, and reach a maximum before it decreases again. This suggests that the absence of $Al_2O_3$ significantly increases the susceptibility of molten glass to devitrification at temperatures relevant to the conditioning of commercial soda-lime-silica melts, and therefore the presence of even small amounts of $Al_2O_3$ can notably improve conditioning of commercial container and float glass melts by improving $\Delta T = (T_{3.7} - T_{Liq})$ values.

Overall, the bulk crystal fraction of the studied soda-lime-silica glass melts exposed to temperatures 30°C below their liquidus temperatures does vary with composition but this variance appears to be small and is less sensitive to glass composition when considered against the wide range of compositional modifications studied here. However, glasses that fall into the devitrite primary phase field with high bulk crystal fractions should be excluded. Furthermore, the residence times during which glass melts are exposed to subliquidus or liquidus temperatures would be critical; however, glass melts with $\Delta T = 0$ might be beneficiated in

hollowware processes, in which one of the highest cooling rates of 40-80°C/s are applied.[40] On the other hand, slightly positive $\Delta T$ values can also be considered for float glass processes by increasing CaO/MgO ratios and may still be safe to manufacture, as their cooling rates of 1-3°C/s[37,40] appear to be sufficiently high to avoid devitrification. Reformulation of float glass compositions for $\Delta T$ minimization could thus be exploited for improving the melting and refining properties of float glass.

## 5 | CONCLUSIONS

Young's modulus varies with crystalline polymorph. However, the variation of elastic moduli, particularly plane strain modulus, in corresponding $SiO_2$-$Na_2O$-MgO-CaO-$Al_2O_3$ glass compositions were found to be insignificant over a wide compositional range. In contrast, the brittleness of soda-lime-silica glass varies considerably with composition, and 30% lower brittleness values can be obtained for glasses with compositions within the silica phase field relative to the glasses with the highest brittleness values across the studied compositional range. It is likely that the structural rearrangement occurs as a result of phase transitions in which the fraction of smaller-numbered silicate rings may increase and subsequently give rise to significantly lower brittleness values as is observed in glasses of silica phase fields (Tables A1 and A2).

Even the small addition of $Al_2O_3$ can significantly improve the resistance to crystallization and working properties of soda-lime-silica melts; varying the ratio of CaO/MgO can also substantially modify the crystallization properties of soda-lime-silica glasses with multiple inversion points. Therefore, manipulating CaO/MgO ratios can provide the desired crystallization properties without significantly compromising the forming and melting performance of some soda-lime-silica melts. The rate of bulk crystallization appears not to be a strong function of the composition at temperatures relevant to the conditioning of commercial container and float glass melts, and this may enable minimization of the temperature difference between the working point and liquidus temperature of melts for which sufficiently high cooling rates are applied, thereby potentially enabling lower melting temperatures and thus lower fuel-derived $CO_2$ emissions from future commercial glass melting operations.

## ACKNOWLEDGMENT

EK thanks Gurallar Glass Packaging and LAV Tableware Glass for PhD funding.

## ORCID

*Erhan Kilinc* https://orcid.org/0000-0002-5280-0275
*Paul A. Bingham* https://orcid.org/0000-0001-6017-0798
*Russell J. Hand* https://orcid.org/0000-0002-5556-5821

## REFERENCES

1. Rouxel T. Driving force for indentation cracking in glass: composition, pressure and temperature dependence. Philos Trans A Math Phys Eng Sci. 2015;373(2038):20140140.
2. Wiederhorn SM. Fracture surface energy of glass. J Am Ceram Soc. 1969;52(2):99–105.
3. Hand RJ, Tadjiev DR. Mechanical properties of silicate glasses as a function of composition. J Non-Cryst Solids. 2010;356(44–49):2417–23.
4. Sehgal J, Ito S. A new low-brittleness glass in the soda-lime-silica glass family. J Am Ceram Soc. 1998;81(9):2485–8.
5. Dejneka MJ, Ellison AJ, Gomez S, Morena RM. Corning Incorporated. Glasses having improved toughness and scratch resistance. U.S. Patent 8,969,226. 2015.
6. Kilinc E, Hand RJ. Mechanical properties of soda–lime–silica glasses with varying alkaline earth contents. J Non-Cryst Solids. 2015;429:190–7.
7. Dériano S, Jarry A, Rouxel T, Sangleboeuf JC, Hampshire S. The indentation fracture toughness ($K_C$) and its parameters: the case of silica-rich glasses. J Non-Cryst Solids. 2004;344(1–2):44–50.
8. Babcock CL. Substructure classification of silicate glasses. J Am Ceram Soc. 1969;52(3):151–3.
9. Georoff AN, Babcock CL. Relation of microindentation hardness to glass composition. J Am Ceram Soc. 1973;56(2):97–9.
10. Morey GW. The devitrification of soda-lime-silica glasses[1]. J Am Ceram Soc. 1930;13(10):683–713.
11. Morey GW. The effect of boric oxide on the devitrification of the soda-lime-silica glasses. The quaternary system, $Na_2O$-CaO-$B_2O_3$-$SiO_2$[1]. J Am Ceram Soc. 1932;15(9):457–75.
12. Silverman WB. Effect of alumina on devitrification of soda-lime-silica glasses. J Am Ceram Soc. 1939;22(1–12):378–84.
13. Silverman WB. Effect of alumina on devitrification of sodium oxide-dolomite Lime-silica glasses. J Am Ceram Soc. 1940;23(9):274–81.
14. Swift HR. Effect of magnesia and alumina on rate of crystal growth in some soda-lime-silica glasses. J Am Ceram Soc. 1947;30(6):170–4.
15. Contribution of the general research laboratory owens-illinois glass company. Effect of barium oxide and zinc oxide on properties of soda-dolomite – lime – silica glass. J Am Ceram Soc. 1942;25(3):61–9.
16. Owens-Illinois Glass Company General Research Laboratory. Effect of substituting MgO for CaO on properties of typical soda-lime glasses. J Am Ceram Soc. 1944;27(8):221–5.
17. Contribution of the Owens-Illinois Glass Company General Research Laboratory. Effect of boric oxide on properties of soda-dolomitic lime-silica glasses. J Am Ceram Soc. 1948;31(1):8–14.
18. Hrma P, Smith DE, Matyáš J, Yeager JD, Jones JV, Boulos EN. Effect of float glass composition on liquidus temperature and devitrification behaviour. Glass Technol-Eur J Glass Sci Technol Part A. 2006;47(3):78–90.
19. Bingham PA, Marshall M. Reformulation of container glasses for environmental benefit through lower melting temperatures. Glass Technol. 2005;46(1):11–9.
20. Fluegel A. Glass viscosity calculation based on a global statistical modelling approach. Glass Technol-Eur J Glass Sci Technol Part A. 2007;48(1):13–30.
21. Rouxel T. Elastic properties and short-to medium-range order in glasses. J Am Ceram Soc. 2007;90(10):3019–39.

22. Shannon RD. Revised effective ionic radii and systematic studies of interatomic distances in halides and chalcogenides. Acta Crystallographica Sec A. 1976;32(5):751–67.
23. Hrma PR, Vienna JD, Mika M, Crum JV, Piepel GF. Liquidus Temperature Data for DWPF Glass. Richland, WA: Pacific Northwest National Lab; 1998.
24. Standard AS. Standard practices for measurement of liquidus temperature of glass by the gradient furnace method, Annual Book of ASTM Standards, C 829–81. Gaithersburg: American Society for Testing and Materials; 1990.
25. International Centre for Diffraction Data. [Internet]. 12 Campus Blvd, Newtown Square, PA 19073, USA [Cited 2020 September 15]. Available from: www.icdd.com.
26. Rietveld H. A profile refinement method for nuclear and magnetic structures. J Appl Crystallogr. 1969;2(2):65–71.
27. Rodríguez-Carvajal J. Recent advances in magnetic structure determination by neutron powder diffraction. Phys B. 1993;192(1–2):55–69.
28. Xrd.us [Internet]. 52 Papania Drive, Mahopac, New York 10541 USA [updated 2005 March 03; cited 2020 September 15]. Available from: https://www.xrd.us/technote/amorphous%20content%20determination.htm.
29. Colomban P, Tournié A, Bellot-Gurlet L. Raman identification of glassy silicates used in ceramics, glass and jewellery: a tentative differentiation guide. J Raman Spectrosc. 2006;37(8):841–52.
30. Le Losq C, Neuville DR, Florian P, Henderson GS, Massiot D. The role of $Al^{3+}$ on rheology and structural changes in sodium silicate and aluminosilicate glasses and melts. Geochim Cosmochim Acta. 2014;126:495–517.
31. Standard BS EN ISO. 18756. Fine ceramics (advanced ceramics, advanced technical ceramics)-Determination of fracture toughness of monolithic ceramics at room temperature by the surface crack in flexure (SCF) method; 2005.
32. Glaesemann GS, Ritter JE Jr, Jakus K. Mixed-mode fracture in soda-lime glass using indentation flaws. J Am Ceram Soc. 1987;70(9):630–6.
33. Yoda M. Subcritical crack growth of glass. Eng Fract Mech. 1987;28(1):77–84.
34. Samuel R, Chandrasekar S, Farris TN, Licht RH. Effect of residual stresses on the fracture of ground ceramics. J Am Ceram Soc. 1989;72(10):1960–6.
35. Quinn GD, Salem JA. Effect of lateral cracks on fracture toughness determined by the surface-crack-in-flexure method. J Am Ceram Soc. 2002;85(4):873–80.
36. Lawn BR, Marshall DB. Hardness, toughness, and brittleness: an indentation analysis. J Am Ceram Soc. 1979;62(7–8):347–50.
37. Wallenberger FT, Bingham PA. Fiberglass and glass technology. Energy-Friendly Compositions And Applications. Springer; 2010.
38. Deng W, Spathi C, Coulbeck T, Erhan K, Backhouse D, Marshall M, et al. Exploratory research in alternative raw material sources and reformulation for industrial soda-lime-silica glass batches. Int J Appl Glass Sci. 2020;11(2):340–56.
39. Williams HP. The Influence of chemical composition on the working properties of container glass. Glasteknisk Tidskrift. 1982;37(3):77-82.
40. Wallenberger FT, Smrček A. The liquidus temperature; its critical role in glass manufacturing. Int J Appl Glass Sci. 2010;1(2):151–63.
41. Mauro JC, Yue Y, Ellison AJ, Gupta PK, Allan DC. Viscosity of glass-forming liquids. Proc Natl Acad Sci. 2009;106(47):19780–4.
42. Cuartas R. Calculo teorico de propiedades del vidrio: viscosidad, parametros termicos y parametros de desvitrificacion. Ceramica et Vidrio. 1984;23:105–11.
43. Babcock CL. Silicate glass technology methods. New York: John Wiley; 1977.
44. Šašek L, Bartuška M, Van Thong V. Utilization of mathematicostatistical methods in silicate research. 2. Determination of mathematical relations for the calculation of crystallization properties from chemical composition of sheet and container glass (in Czech). Silikaty. 1973;17(3):207–17.
45. Karlsson KH, Backman R, Hupa L. Models for liquidus temperatures. In Proceedings of the VI European Glass Society Conference. Montpellier, 2002. Available from: http://kdsolution.com/pdf_upload/Karlsson.pdf (Last accessed on 10/02/2021)
46. Fluegel A. Modeling of glass liquidus temperatures using disconnected peak functions. In ACerS 2007 Glass and Optical Materials Division Meeting. http://glassproperties.com/liquidus, 2007.
47. Dreyfus C, Dreyfus G. A machine learning approach to the estimation of the liquidus temperature of glass-forming oxide blends. J Non-Cryst Solids. 2003;318(1–2):63–78.
48. Moir GK, Glasser FP. Phase equilibria in the glass-forming region of the system $Na_2O$-CaO-$Al_2O_3$-$SiO_2$. Phys Chem Glasses. 1976;17(3):45–53.
49. Shahid KA, Glasser FP. Phase equilibria in the glass forming region of the system $Na_2O$-CaO-$SiO_2$. Phys Chem Glasses. 1971;12(2):50–7.
50. Morey GW. The effect of alumina on the devitrification of a soda-lime-silica glass[1]. J Am Ceram Soc. 1930;13(10):718–23.
51. Shahid KA, Glasser FP. Phase equilibria in the glass forming region of the system $Na_2O$-CaO-MgO-$SiO_2$. Phys Chem Glasses. 1972;13(2):27–42.
52. Morey GW. The effect of magnesia on the devitrification of a soda-lime-silica glass[1]. J Am Ceram Soc. 1930;13(10):714–7.
53. Kamita K, Yamamoto H, Matsuo M, Yagai H, Ota H. 'The chemical composition of glasses suitable for the manufacture of window glass by the automatic drawing process. J Soc Glass Technol. 1936;20(80):170–80.
54. Beerkens RG, Conradt R. Round robin test on liquidus temperature of soda–lime–magnesia–silica float glass samples: A technical report of the ICG Technical Committee (TC 18) on Properties of Glass Forming Melts. Glass Technol-Eur J Glass Sci Technol Part A. 2008;49(5):205–12.
55. Backman R, Karlsson KH, Cable M, Pennington NP. Model for liquidus temperature of multi-component silicate glasses. Phys Chem Glasses. 1997;38(3):103–9.
56. Zanotto ED. Surface crystallization kinetics in soda-lime-silica glasses. J Non-Cryst Solids. 1991;129(1–3):183–90.
57. Pabst W, Gregorová EV. Elastic properties of silica polymorphs-a review. Ceram-Silik. 2013;57(3):167–84.
58. Ewalds HL, Wanhill RJH. Fracture Mechanics. London, UK: Edward Arnold; 1984.
59. Philipps K, Stoffel RP, Dronskowski R, Conradt R. Experimental and theoretical investigation of the elastic moduli of silicate glasses and crystals. Front Mater. 2017;4:2.
60. Lin CC, Leung KS, Shen P, Chen SF. Elasticity and structure of the compounds in the wollastonite ($CaSiO_3$)-$Na_2SiO_3$ system: from amorphous to crystalline state. J Mater Sci - Mater Med. 2015;26(1):39.
61. Aleksandrov KS, Ryzhova TV, Belikov BP. The elastic properties of pyroxenes. Soviet Physics Crystallography. 1964;8(5):589–91.
62. Sehgal J, Ito S. Brittleness of glass. J Non-Cryst Solids. 1999;253(1–3):126–32.

63. Arora A, Marshall DB, Lawn BR, Swain MV. Indentation deformation/fracture of normal and anomalous glasses. J Non-Cryst Solids. 1979;31(3):415–28.
64. Kilinc E. Mechanical and structural properties of soda lime silica glasses as a function of composition (Doctoral dissertation. University of Sheffield); 2016.
65. Shi Y, Neuefeind J, Ma D, Page K, Lamberson LA, Smith NJ, et al. Ring size distribution in silicate glasses revealed by neutron scattering first sharp diffraction peak analysis. J Non-Cryst Solids. 2019;516:71–81.
66. Jialiang YI. Further studies on the IR spectra of silicate glasses. J Non-Cryst Solids. 1986;84(1–3):114–9.
67. Hehlen B, Neuville DR. Raman response of network modifier cations in alumino-silicate glasses. J Phys Chem B. 2015;119(10):4093–8.
68. Ito S, Taniguchi T, Ono M, Uemura K. Network and void structures for glasses with a higher resistance to crack formation. J Non-Cryst Solids. 2012;358(24):3453–8.
69. Bingham PA. The effects of 1 wt% $P_2O_5$ addition on the properties of container glass. Glass Technol. 2004;45(6):255–8.
70. Veit U, Rüssel C. Viscosity and liquidus temperature of quaternary glasses close to an eutectic composition in the CaO-MgO-$Al_2O_3$-$SiO_2$ system. J Mater Sci. 2017;52(13):8280–92.
71. Scaglioni O. Marble and dolomite in commercial glasses and the trends characterizing the present vitrifiable compositions. Vetro Informazione. 1984, Marzo - Aprile; N, 20.

**How to cite this article:** Kilinc E, Bell AM, Bingham PA, Hand RJ. Effects of composition and phase relations on mechanical properties and crystallization of silicate glasses. *J Am Ceram Soc*. 2021;104:3921–3946. https://doi.org/10.1111/jace.17784

## APPENDIX A

**TABLE A1** Unit cell parameters for tridymite identified in devitrified serial glasses

| | | | Tridymite $SiO_2$-Cc | | | | |
|---|---|---|---|---|---|---|---|
| **Glass ID** | **Crystal Phases** | **Anode** | **a** | **b** | **c** | **beta** | **V** |
| $A_0S_{75}N_{12}$ | T + C | Cu | 18.4015 (15) | 5.0021 (3) | 23.9788 (18) | 106.207 (4) | 2119.4 (3) |
| $A_{0.5}S_{74}N_{12.5}$ | C + T | Cu | 18.434 (3) | 4.9658 (4) | 24.124 (6) | 105.699 (11) | 2126.0 (7) |

**TABLE A1** continued. Unit cell parameters for cristobalite identified in devitrified serial glasses

| | Cristobalite $SiO_2$ - $P4_12_12$ | | |
|---|---|---|---|
| **Glass ID** | **a** | **c** | **V** |
| $A_0S_{75}N_{12}$ | 4.979 (2) | 7.027 (6) | 174.23 (20) |
| $A_{0.5}S_{74}N_{12.5}$ | 4.9825 (3) | 6.9360 (7) | 172.18 (2) |
| $M_0S_{75}$ | 4.9920 (9) | 6.928 (3) | 172.64 (8) |
| $M_1S_{74}$ | 4.9955 (18) | 6.943 (5) | 173.26 (14) |
| $M_2S_{73}$ | 4.9952 (14) | 6.962 (4) | 173.71 (12) |
| $C_7S_{75}$ | 4.9864 (7) | 6.9385 (17) | 172.52 (5) |
| $C_8S_{74}$ | 4.9996 (8) | 6.911 (2) | 172.74 (6) |
| $C_9S_{73}$ | 4.9761 (9) | 7.0723 (17) | 175.12 (6) |
| $M_5C_8$ | 4.9983 (14) | 6.928 (4) | 173.07 (12) |

**TABLE A1** continued. Unit cell parameters for devitrite identified in devitrified serial glasses

| | Devitrite $Na_2Ca_3$ ($Si_6O_{16}$)-P−1 | | | | | | |
|---|---|---|---|---|---|---|---|
| **Glass ID** | **a** | **b** | **c** | **alpha** | **beta** | **gamma** | **V** |
| $M_1S_{74}$ | 7.2251 (3) | 10.1879 (7) | 10.6883 (7) | 95.608 (4) | 109.769 (4) | 99.402 (4) | 720.46 (8) |

**TABLE A1** continued. Unit cell parameters for Wollastonite - 1A identified in devitrified serial glasses

| | Wollastonite-*1A* $CaSiO_3$ – P-1 | | | | | | |
|---|---|---|---|---|---|---|---|
| **Glass ID** | **a** | **b** | **c** | **alpha** | **beta** | **gamma** | **V** |
| $A_{2.5}S_{70}N_{14.5}$ | 7.9264 (4) | 7.3305 (6) | 7.0634 (4) | 90.071 (10) | 95.163 (8) | 103.538 (7) | 397.29 (4) |
| $A_{3.5}S_{68}N_{15.5}$ | 7.9263 (4) | 7.3272 (4) | 7.0628 (4) | 90.081 (9) | 95.204 (7) | 103.475 (6) | 397.15 (4) |
| $A_{4.5}S_{66}N_{16.5}$ | 7.9190 (3) | 7.3213 (3) | 7.0648 (3) | 90.318 (6) | 95.092 (4) | 103.325 (4) | 396.85 (3) |
| $M_4S_{71}$ | 7.9215 (4) | 7.3259 (4) | 7.0628 (3) | 90.214 (8) | 95.141 (6) | 103.410 (5) | 396.97 (4) |
| $M_5S_{70}$ | 7.9172 (3) | 7.3203 (4) | 7.0577 (3) | 90.062 (8) | 95.191 (4) | 103.357 (5) | 396.24 (3) |
| $C_8S_{74}$ | 7.8975 (16) | 7.327 (2) | 7.0564 (15) | 90.01 (3) | 94.81 (3) | 102.93 (3) | 396.47 (17) |
| $C_9S_{73}$ | 7.9234 (5) | 7.3282 (8) | 7.0665 (5) | 90.241 (12) | 95.015 (10) | 103.412 (12) | 397.46 (6) |
| $C_{11}S_{71}$ | 7.9245 (4) | 7.3241 (3) | 7.0643 (3) | 90.201 (6) | 95.222 (5) | 103.403 (4) | 397.06 (3) |
| $C_{13}S_{69}$ | 7.9265 (3) | 7.3232 (3) | 7.0629 (2) | 90.052 (6) | 95.192 (4) | 103.503 (3) | 396.91 (3) |
| $C_{14}S_{68}$ | 7.9283 (5) | 7.3279 (5) | 7.0642 (4) | 90.011 (10) | 95.183 (8) | 103.449 (7) | 397.43 (4) |
| $M_1C_{12}$ | 7.9271 (4) | 7.3340 (4) | 7.0659 (3) | 90.053 (9) | 95.186 (7) | 103.457 (6) | 397.78 (4) |

**TABLE A1** continued. Unit cell parameters for Wollastonite - *2M* identified in devitrified serial glasses

| | Wollastonite-2M $CaSiO_3$ - $P2_1/a$ | | | | |
|---|---|---|---|---|---|
| **Glass ID** | **a** | **b** | **c** | **beta** | **V** |
| $A_{1.5}S_{72}N_{13.5}$ | 15.4217 (12) | 7.3198 (4) | 7.0635 (4) | 95.353 (7) | 793.88 (9) |
| $M_2S_{73}$ | 15.4290 (10) | 7.3221 (4) | 7.0658 (4) | 95.385 (6) | 794.72 (8) |
| $M_3S_{72}$ | 15.4217 (12) | 7.3198 (4) | 7.0635 (4) | 95.353 (7) | 793.88 (9) |
| $M_6S_{69}$ | 15.4068 (8) | 7.3152 (3) | 7.0562 (3) | 95.368 (5) | 791.77 (7) |
| $C_{10}S_{72}$ | 15.4217 (12) | 7.3198 (4) | 7.0635 (4) | 95.353 (7) | 793.88 (9) |
| $C_{12}S_{70}$ | 15.4123 (6) | 7.3226 (2) | 7.0653 (3) | 95.345 (3) | 793.90 (5) |
| $M_3C_{10}$ | 15.4217 (12) | 7.3198 (4) | 7.0635 (4) | 95.353 (7) | 793.88 (9) |
| $M_5C_8$ | 15.412 (2) | 7.3158 (8) | 7.0577 (8) | 95.360 (13) | 792.29 (17) |

**TABLE A1** continued. Unit cell parameters for diopside identified in devitrified serial glasses

| | Diopside $CaMgSi_2O_6$ - C2/c | | | | |
|---|---|---|---|---|---|
| **Glass ID** | **a** | **b** | **c** | **beta** | **V** |
| $M_7S_{68}$ | 9.7458 (5) | 8.9217 (5) | 5.2477 (3) | 105.868 (4) | 438.90 (4) |
| $M_7C_6$ | 9.7447 (19) | 8.9287 (17) | 5.2497 (9) | 105.843 (14) | 439.41 (14) |
| $M_9C_4$ | 9.7429 (3) | 8.9216 (3) | 5.24479 (16) | 105.888 (2) | 438.47 (2) |
| $M_{11}C_2$ | 9.7370 (4) | 8.9201 (3) | 5.24193 (19) | 106.017 (2) | 437.61 (3) |

**TABLE A2** Goodness of fit parameters of Rietveld refined serial glass

| Glass ID | $R_p$ | $R_{wp}$ | $R_{exp}$ | $\chi^2$ |
|---|---|---|---|---|
| $A_0S_{75}N_{12}$ | 49.3 | 26.5 | 15.2 | 3.06 |
| $A_{0.5}S_{74}N_{12.5}$ | 41.3 | 16.9 | 12 | 2.03 |
| $A_{1.5}S_{72}N_{13.5}$ | 63.5 | 27.1 | 22 | 1.53 |
| $A_{2.5}S_{70}N_{14.5}$ | 43.6 | 15.7 | 11.8 | 1.76 |
| $A_{3.5}S_{68}N_{15.5}$ | 52.2 | 22.9 | 16.7 | 1.87 |
| $A_{4.5}S_{66}N_{16.5}$ | 32.5 | 17.8 | 12.7 | 1.98 |
| $M_0S_{75}$ | 83 | 22.4 | 19.6 | 1.58 |
| $M_1S_{74}$ | 30.3 | 30 | 8.83 | 11.54 |
| $M_2S_{73}$ | 43.9 | 16.7 | 13 | 1.67 |
| $M_3S_{72}$ | 63.5 | 27.1 | 22 | 1.53 |
| $M_4S_{71}$ | 46.3 | 18.6 | 13.7 | 1.85 |
| $M_5S_{70}$ | 34.4 | 19.2 | 12 | 2.58 |
| $M_6S_{69}$ | 49.6 | 23.1 | 16.1 | 2.07 |
| $M_7S_{68}$ | 108 | 38.9 | 39.5 | 1.1 |
| $C_7S_{75}$ | 78.4 | 22.7 | 19.2 | 1.69 |
| $C_8S_{74}$ | 91.2 | 20 | 11.8 | 3.03 |
| $C_9S_{73}$ | 55.7 | 21.7 | 15.4 | 1.97 |
| $C_{10}S_{72}$ | 63.5 | 27.1 | 22 | 1.53 |
| $C_{11}S_{71}$ | 47.4 | 24.2 | 14.6 | 2.75 |
| $C_{12}S_{70}$ | 36.7 | 21.7 | 14 | 2.43 |
| $C_{13}S_{69}$ | 72.9 | 33 | 21.9 | 2.34 |
| $C_{14}S_{68}$ | 51.9 | 27.1 | 13.3 | 4.12 |
| $M_1C_{12}$ | 43.7 | 18.8 | 13.4 | 1.99 |
| $M_3C_{10}$ | 63.5 | 27.1 | 22 | 1.53 |
| $M_5C_8$ | 30.7 | 10.5 | 7.73 | 1.86 |
| $M_7C_6$ | 212 | 38.4 | 34.4 | 1.5 |
| $M_9C_4$ | 47.3 | 20.5 | 16.5 | 1.74 |
| $M_{11}C_2$ | 61.2 | 27.1 | 23.6 | 1.48 |

## APPENDIX B

For fracture toughness measured by SCF method (Newman and Raju, 1981).

$Y_{max}$ is the greater value of either $Y_s$ or $Y_d$ which are given by

$$Y_d = \left(\sqrt{\pi} M H_2\right) / \sqrt{Q}$$

$$Y_s = \left(\sqrt{\pi} M X H_1\right) / \sqrt{Q}$$

where

$$Q = 1 + 1.464\,(a/c)^{1.65}$$

$$M = \left[1.13 - 0.09\,(a/c)\right] + \left\{-0.54 + 0.89\left[0.2 + (a/c)^{-1}\right]\right\}(a/L)^2 + \left\{0.5 - \left[0.65 + (a/c)\right]^{-1} + 14\,(1 - a/c)^{24}\right\}(a/L)^4$$

$$H_1 = 1 - \left[0.34 + 0.11\,(a/c)\right](a/L)$$

$$H_2 = 1 - \left[1.22 + 0.12\,(a/c)\right](a/L) + \left[0.55 - 1.05\,(a/c)^{0.75} + (a/c)^{1.5}\right](a/L)^2$$

$$X = \left[1.1 + 0.35\,(a/L)^2\right]\sqrt{a/c}$$

$$F = \left(F_O - F_i\right)/2$$

Where $a$ and $c$ are the crack depth and crack half width in meters, respectively.

$L$ is the depth of specimen in millimeters.

$H_1$ is polynomial in the stress intensity factors coefficients which arises on the crack periphery where intersects the sample surface.

$H_2$ is the polynomial in the stress intensity factors coefficients which arises at the bottom end of the surface crack.

$M$ is also polynomial in the stress intensity factors coefficients.

$X$ is a factor in the stress intensity factor coefficient.

$Q$ is a polynomial function of the surface crack ellipticity.

$F$ is the four-point fixture moment arm in millimeters, and $F_o$ and $F_i$ are the outer and inner spans, respectively.